Macromolecular Materials and Engineering

Macromolecular Materials and Engineering Open Access
www.mame-journal.de

REVIEW OPEN ACCESS

Warpage in Material Extrusion Additive Manufacturing of Amorphous and Semicrystalline Polymers

Ali Zerriouh[1] | Amani Deghiche[2] | Walid Benayache[3] | Targol Hashemi[4] | Alessandra Bernardi[5] | Sara Liparoti[4] | Maria Laura Di Lorenzo[5] | Dario Cavallo[1]

[1]Department of Chemistry and Industrial Chemistry, University of Genova, via Dodecaneso 31, Genova, Italy | [2]Laboratoire de Physico-Chimie des Hauts Polymères (LPCHP), Département de Génie des Procédés, Faculté de Technologie, Université Ferhat ABBAS Sétif-1, Sétif, Algeria | [3]Laboratory of Preparation, Modification, and Applications of Multiphase Polymeric Materials (LMPMP), Process Engineering Department, Faculty of Technology, Ferhat Abbas Setif-1 University, Setif, Algeria | [4]Department of Industrial Engineering, University of Salerno, via Giovanni Paolo II, 132, Fisciano, SA, Italy | [5]Institute of Polymers, Composites and Biomaterials (IPCB), National Research Council (CNR), Via Campi Flegrei, 34, Pozzuoli, NA, Italy

Correspondence: Sara Liparoti (sliparoti@unisa.it) | Maria Laura Di Lorenzo (marialaura.dilorenzo@cnr.it) | Dario Cavallo (dario.cavallo@unige.it)

Received: 22 April 2025 | **Revised:** 14 July 2025 | **Accepted:** 16 July 2025

Funding: This work received financial support from European Union–Next Generation EU–PNRR M4/C2/INVESTIMENTO.1.1, in the frame of the PRIN 2022 programme (D.D. 104, 02-02-2022), Project 2022MMTBMJ "Zero-defect Fused Filament Fabrication" (0DeF3), ERC field PE11, CUP D53D23005420006.

Keywords: 3D printing | additive manufacturing | material extrusion | warpage

ABSTRACT

Material Extrusion Additive Manufacturing (MEAM) offers the ability to manufacture complex geometries through layer-by-layer deposition. MEAM involves fast heating and cooling of polymers, processes that involve thermal expansion and contraction of materials that may undergo phase transitions. These phenomena may lead to warpage: distortion of the printed parts or deviation from the intended geometry, which significantly compromises the dimensional accuracy and functionality of parts. Mitigation or even cancelling warpage has become one of the roadblocks toward further widespread application of MEAM technology, a target that requires a thorough understanding of the phenomenon. To contribute to this goal, this review presents and discusses the current knowledge of warpage in MEAM, starting with a general presentation of the technology and its intrinsic features, followed by details of the fundamental mechanisms of warpage, highlighting the crucial interaction between processing parameters, material characteristics, and part geometry. A thorough analysis of the experimental methodologies used to quantify warpage is presented, alongside a comparative exploration of warpage behavior in amorphous and semicrystalline polymers. The state-of-the-art of current modeling approaches aimed at predicting the warpage phenomenon is also presented and discussed, with a focus on the capability to effectively consider the complex thermo–mechanical history specific to MEAM.

Abbreviations: 3D printing, Three-dimensional printing; ABS, Acrylonitrile-butadiene-styrene; AM, Additive manufacturing; ANOVA, Analysis of variance; CCD, Charge-coupled device; DIC, Digital image correlation; EOC, Poly(ethylene-*co*-octene) copolymer; EVA, Poly(ethylene-*co*-vinyl acetate) copolymer; FEA, Finite Element Analysis; FFF, Fused filament fabrication; FGF, Fused granule fabrication; G, Crystal growth rate; h, Height; l, Length; MEAM, Material extrusion additive manufacturing; P4MP1, Poly(4-methylpentene-1); PA, Polyamide; PB, Isotactic Poly(butene-1); PC, Polycarbonate; PLA, Poly(lactic acid); PEEK, Polyetheretherketone; PET, Poly(ethylene terephthalate); PET-G, Poly(ethylene terephthalate)-glycol; POE-*g*-MAH, Maleic anhydride grafted poly(ethylene-*co*-1-octene) copolymer; PP, Isotactic polypropylene; PS, Polystyrene; PTT, Poly(trimethylene terephthalate); PTTIS, Poly(trimethylene terephthalate-*co*-isophthalate-*co*-sebacate units; PVT, Pressure-volume-temperature; T_b, Deposition plate temperature; T_n, Nozzle temperature; TPU, Thermoplastic polyurethane; X_c, Degree of crystallinity; w, Width; δ, Flatness error; λ_{B0}, Bragg wavelength; n_{eff}, Effective refractive index of the fiber core; ε_{res}, Fabrication induced residual strains; Λ, Periodic spacing of the grating; Pe, Strain-optic coefficient of the fiber; ε_{ii}, Strain component; σ, Stress; P, Pressure; s_{ii}, The stress components; E, Elastic modulus; β, Linear compressibility; α, Linear thermal expansion coefficient; ξ, Degree of crystallinity; C_{cr}, Linear shrinkage from an amorphous to 100% relative crystalline degree.; ε^P, Material compressibility; T_s, Values of T at the solidification; ξ_s, Values of ξ at the solidification; η_{fr}, Friction factor; $\dot{z}_s$, Rate of formation of the solid layer; t_{sz}, Instant of solidification; δ_y, Shrinkage along with the length directions; δ_x, Shrinkage along with the width directions; δ_z, Total thickness shrinkage; δ_0, Layer thickness; ν, Poisson's ratio.

1 | Introduction

Additive manufacturing (AM), also known as 3D printing, has advanced considerably since its inception in the 1980s. Primarily designed as a fast-prototyping instrument [1, 2], it has gradually developed into a legitimate manufacturing method, including a wide range of applications [3–5]. Technological advances are characterized by innovations in materials, technology, and software, driving the integration of 3D printing into a variety of industries, including aerospace, automotive, healthcare, fashion, etc. [3, 4]. Currently, 3D printing is recognized for its remarkable ability to customize products, minimize waste, and create intricate shapes that are challenging or even unfeasible to produce using traditional manufacturing methods. This transformation made AM a general-purpose technology, having been widened to many types of materials, including polymers, metals, ceramics, and composites. This led to ground-breaking advancements in 3D printing across multiple industrial and technological fields.

The 3D Printer Market Size was valued at USD 2.2 billion in 2024 [6]; it is expected to grow by approximately 15% between 2020 and 2025. The participation of AM in the automotive industry is expected to increase by 36% from 2020 to 2025, 51% in the aerospace and medical industries, and 23% in the printing of various types of devices [7]. Despite the widespread diffusion of AM machines, a gap is recognized between the market potential and the effective utilization of the technology [8]. This gap is likely due to a limited understanding and control of the phenomena that lead to defective parts [9].

Among the various 3D printing processes, material extrusion additive manufacturing (MEAM) is probably the most used polymer-based AM technology [2, 6–8], which has become widely popular after expiration of much of its intellectual property [10, 11]. MEAM constructs 3D objects layer by layer, deposited on a plate through extrusion of filaments (fused filament fabrication, FFF) or granules (fused granule fabrication, FGF) of a thermoplastic polymer. Guided by precise digital control [1], the polymer is heated and extruded to a temperature close to the melting/fluidification point through a heated nozzle [12, 13]. As the polymer fluid overflows upon the preceding layer, the sequence of layers gives shape to the final object.

Compared with other polymer-based additive manufacturing techniques, MEAM can be used with the broadest range of materials, including both amorphous and semicrystalline thermoplastic polymers. Some examples of amorphous polymers frequently employed in MEAM include acrylonitrile-butadiene-styrene (ABS) [14], polycarbonate (PC) [15, 16], or polystyrene (PS) [1] and even elastomers [17]. Semicrystalline polymers used in MEAM comprise, among others, poly(lactic acid)(PLA) [14, 18–20], nylons (polyamide, PA) [21], and polyolefins, e.g., polypropylene (PP) [22, 23].

Thanks to the widespread simplicity of use and its versatility, MEAM brought huge technological innovations, which can be even amplified once a few critical issues are solved, with warpage being probably the most significant one. Warpage is a distortion of the printed part, visible as unevenness or curvature in the material's shape that affects its functionality or aesthetic [19, 24].

Warpage most commonly appears as a significant rise in the height of the bottom parts, as sketched in Figure 1a, where an unwarped 3D printed part that displays straight bottom edges is compared with a warped part, printed with the same planned geometry, but that presents curved bottom edges. To better highlight how significant, even in simple objects, material distortion caused by warpage can be, Figure 1b shows a few examples of sizably warped 3D parts built with filaments made of PP or of PP random copolymers (raco PP), and compared to the same part printed with ABS, where no sizable warpage appears [3, 26, 27].

In this review paper, we provide a comprehensive overview of the factors influencing warpage deformation in additive manufacturing by extrusion of amorphous and semicrystalline polymer materials. The review will cover the following aspects:

- Overview of MEAM
- Warpage in MEAM.
- Experimental determination of warpage
- Warpage of amorphous and semicrystalline polymers
- Modeling of the warpage
- Conclusions and future outlooks

2 | Overview of MEAM

Figure 2 details a typical MEAM process: a thermoplastic polymer is fed, either as solid pellets or filament, melted and extruded via a device that controls the flow rate (pinch-roller in FFF, or screw in FGF), then the extrudate is laid on the deposition plate, cools, and the polymer chains relax to some extent [29]. This is followed by a continuous layout of extruded material, which solidifies and welds on top of the already deposited part, forming the final product. The print head and deposition plate move in the appropriate x–y or z-direction to continue printing until the entire part is created.

Temperature and flow fields into the nozzle influence rheology of the polymers during extrusion. The shear rates of the molten polymer within the nozzle significantly influence polymer chain orientation and molecular stretch [29, 30].

MEAM has an intrinsic non-isothermal nature, and the thermal profile along the whole printing process determines the cooling rate, material shrinking, welding of the layers, and, in turn, warpage. Figure 3 shows the velocity field obtained from the simulation of the extrusion process of ABS. It can be noticed that the velocity is maximum at the center of the nozzle and minimum towards the nozzle wall due to the no-slip boundary condition [31].

The effect of a convergent flow is a molecular stretch of the polymer chains that has to be relaxed at the nozzle exit during deposition. Residual stresses could lead to faster crystallization, which, in turn, could induce part deformation [33].

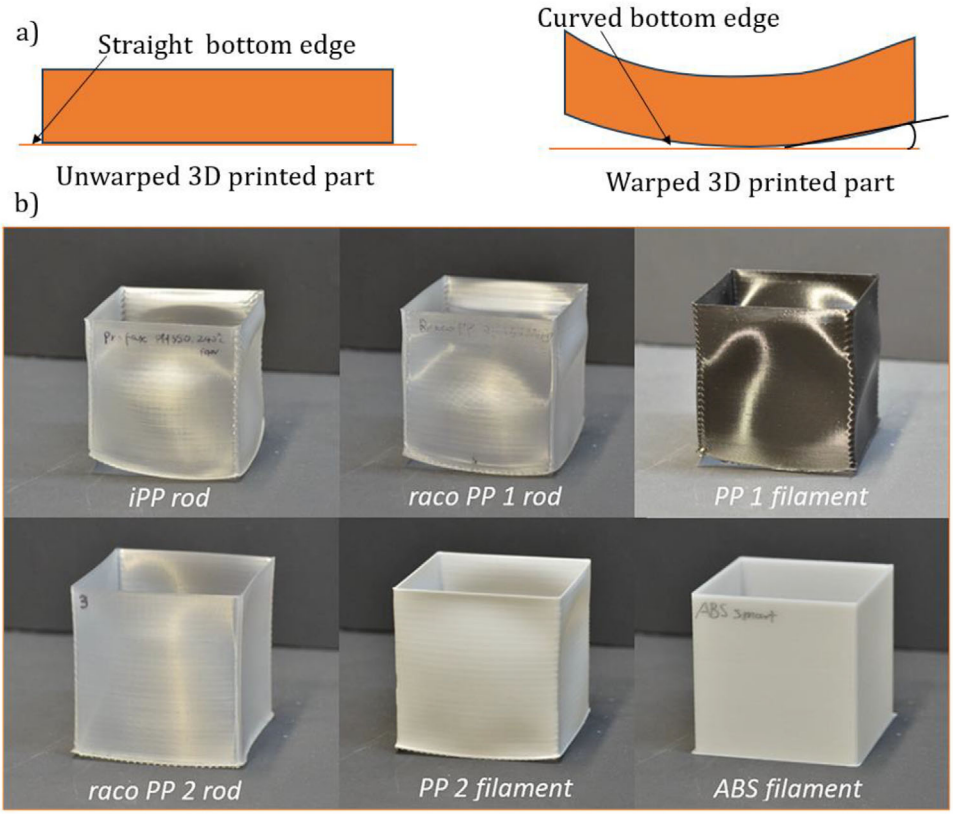

FIGURE 1 | a) Comparison between unwarped and warped printed parts; b) Warped geometries made of different PP grades (homopolymer and random copolymers) compared with ABS. Reproduced from Ref. [28] with permission from Wiley. Copyright (2020).

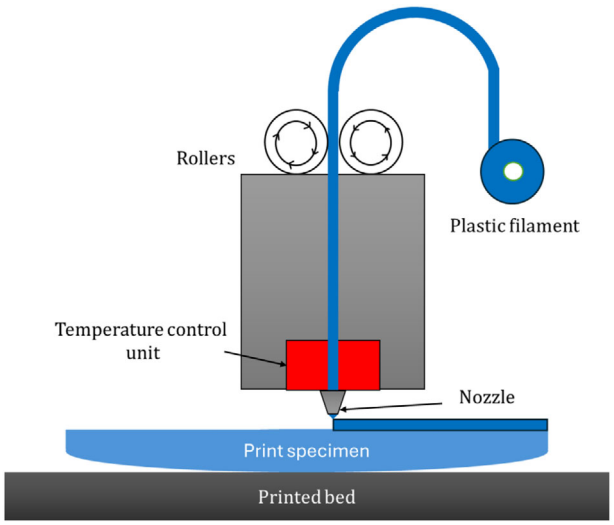

FIGURE 2 | Material extrusion-based 3D printing schematic.

MEAM is characterized by relatively fast cooling, which causes polymers to be frozen in nonequilibrium conformations, insufficient time for molecular mobility at interfaces, and intricate crystallization patterns for semicrystalline polymers [34]. Thermal gradients lead to residual stress: above the glass transition (or crystallization) temperature, stress relaxation occurs fast, whereas below these temperatures, the relaxation time becomes very long. Under high cooling rates, the polymer chains could have insufficient time for relaxation; thus, residual stresses can accumulate. Residual stress increases with cooling rate [35, 36] and may cause deformation of the printed part. Moreover, repeated events of heating and cooling occur every time a molten layer is deposited onto a cooler layer, which creates thermal gradients within the printed part [37, 38], resulting in shrinkage and warpage.

3 | Warpage in MEAM

In thermoplastic polymers, warpage results from complex thermomechanical phenomena occurring during cooling, mainly material shrinkage during cooling, deformation, and detachment from the deposition plate [13, 24, 39, 40]. These processes and phenomena depend on both material properties and process parameters and might be mitigated or even removed via a thorough understanding of warpage in 3D printing, which is, unfortunately, still missing. This is a crucial issue to ensure precise reproduction of the digital model into the printed part, which may allow to widen both applications and employed materials for MEAM, as witnessed by the numerous studies that emphasized the difficulties related to shrinkage and warpage and their effects on printed part deformation [8, 12, 19, 28–30].

Warpage generally occurs to a lower extent in amorphous polymers than in semicrystalline ones. Amorphous polymers are characterized by a random arrangement of the macromolecules,

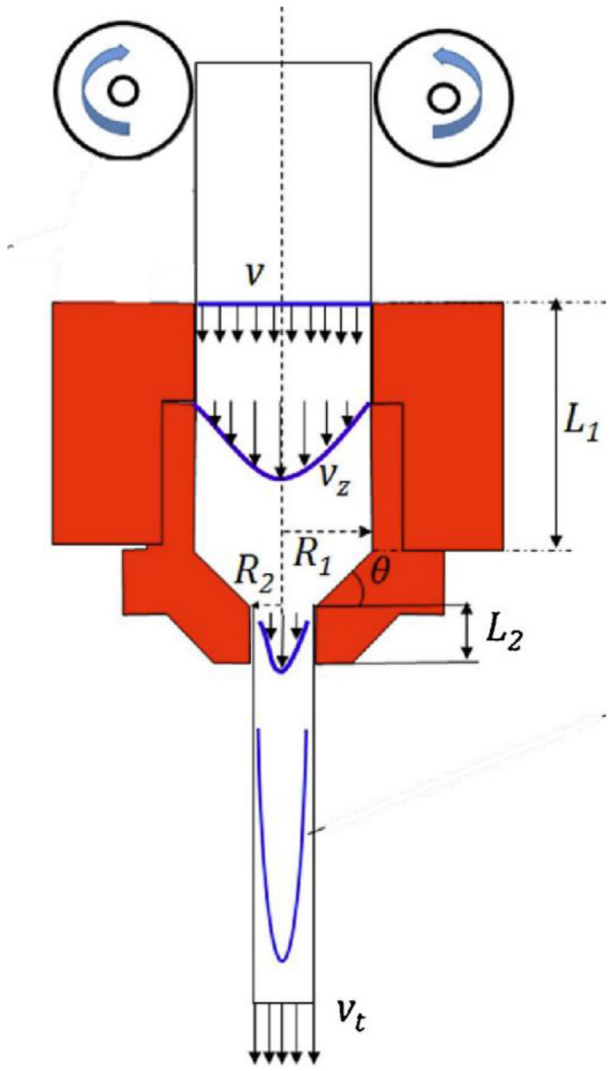

FIGURE 3 | Sketch of velocity field in the liquefier during MEAM of ABS [31, 32]. Adapted from Ref. [32] with permission from Elsevier. Copyright (2018).

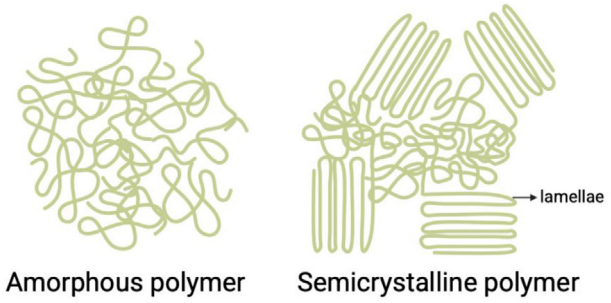

FIGURE 4 | The schematic representation of amorphous and semicrystalline polymers.

which are disorderedly intertwined (see Figure 4) [41, 42]. The main source of material shrinkage in MEAM of amorphous polymers arises from the thermal contraction of the high temperature extruded material to the cooled deposited layer. On the other hand, warpage in semicrystalline polymers is complicated by the formation of crystals upon layer deposition, which may cause part deformation that contributes to the intrinsic volume contraction due to cooling. Semicrystalline polymers have a complex chain arrangement made of ordered structures, organized in thin lamellae, that coexist with disordered amorphous regions: polymer crystallization never reaches completion, and part of the material remains amorphous [30]. This results in an intricate array of ordered and disordered regions, as sketched in Figure 4.

The percentage of material that is in the crystalline state defines the degree of crystallinity (X_c): for typical semicrystalline polymers, X_c generally ranges from 20% to 70% [43] and is influenced by a variety of factors, including molecular weight and the structural characteristics of the polymer chains, like chain regularity. Additionally, processing conditions such as crystallization temperature, cooling rate, applied stress, and the presence of additives play a crucial role in determining the crystallization process. For instance, additives like plasticizers or nucleating agents can hinder or facilitate crystallization, with significant effects on the phase transition kinetics [44–46].

Crystal formation during cooling is only one of the multiplicity of events that can cause dimensional alterations during MEAM, manifesting as either shrinkage or warpage; hence, semicrystalline polymers typically experience more pronounced deformation compared to the amorphous ones [47]. Besides thermal contraction, which also occurs in amorphous polymers, semicrystalline polymers face additional shrinkage caused by crystallization, because the crystalline phase is most often denser than the amorphous phase, and this density variation creates internal shear stresses between layers, leading to increased warpage [38]. Moreover, crystal formation is an exothermic phase transition, which may give rise to uneven cooling and cause temperature gradients between layers, potentially resulting in delamination.

The huge influence of crystal formation on shrinkage is illustrated in Figure 5, which sketches typical pressure–volume–temperature (PVT) plots for amorphous and semicrystalline polymers. As shown in Figure 5, the specific volume of amorphous polymers increases linearly with both temperature and pressure, showing only a varied dependence in correspondence with the glass transition temperature (T_g). Conversely, besides the influence of T_g, in semicrystalline polymers, the specific volume is additionally affected by crystallization and displays an abrupt change upon crystal formation [48–50].

In general, increased crystallinity in polymers results in higher shrinkage [51]; therefore, amorphous polymers, or polymers that crystallize to a very minor extent (5–10%), are often preferred in MEAM. To mitigate the influence of crystallization on material shrinkage and dimensional accuracy, the temperature profile in MEAM printers is often controlled by using a heated deposition plate or a closed chamber, with the related effects on warpage discussed below [52, 53]. In fact, crystallization during manufacturing is influenced by the cooling rate, along with the inherent thermal characteristics of the material, primarily thermal conductivity and specific heat. For example, rapid cooling can inhibit the formation of crystals, thus decreasing shrinkage and warpage [54, 55].

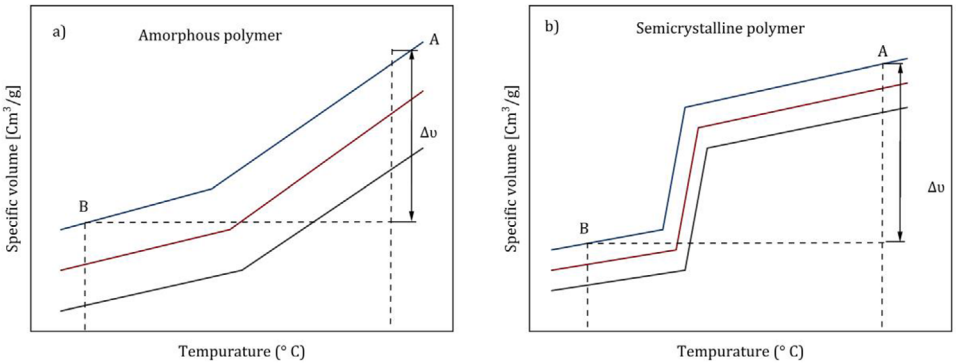

FIGURE 5 | Sketch of the pressure–volume–temperature (PVT) curves for a) amorphous polymer and b) semicrystalline polymers; point A is the processing state and point B is the final state.

4 | Experimental Determination of Warpage

Quantitative analysis of warpage of 3D printed materials is crucial to grasp the main phenomena involved in part deformation and optimize MEAM process, to guarantee the quality and precision of the manufactured parts. Warpage can be measured ex situ, via evaluation of the geometry of the printed part after the process has been completed, or in situ, with real-time analysis of specific parameters, performed during the printing process. The following paragraphs present and discuss both procedures.

4.1 | Ex Situ Warpage Measurements

Recent studies [56, 57] reviewed literature work aimed at measuring, predicting, and controlling various types of geometric error in parts produced by additive manufacturing. The geometry of the part has a predominant impact on warpage. When conducting benchmark studies on warping in 3D printing, specific geometries are often used to analyze and quantify the extent of warpage under different printing conditions. These benchmark geometries are standardized shapes that enable researchers and engineers to compare warpage as a function of materials, printers, and process parameters. Deviations from specified dimensions have been shown to depend on process choices, such as layer thickness, build orientation, and deposition parameters [25, 58–60]. Figure 6 illustrates the main geometries used for this purpose, with main features detailed below, then summarized in Table 1.

4.1.1 | Flat Rectangular Plate and Cube/Parallelepiped

Flat rectangular plates, shown in blue in Figure 6, are the predominant shape used to evaluate warpage in MEAM. The samples typically consist of thin, planar components fabricated in a rectangle or square configuration [25]. The simple design makes them susceptible to out-of-plane deformation (bending or curling) during cooling, thus providing a straightforward model to quantify warpage [25, 61]. The cubic or parallelepiped geometry displays similar features of the flat rectangular plate geometry, with the additional advantage that it allows for carry out study on the effect of the number of layers on warpage. Several studies [25, 38, 62] selected these geometries to investigate warpage, for their simplicity in design and printing, and also to allow easy detection of edge lifting and measurement of warpage.

The main parameters that quantify warpage in flat rectangular geometries include the flatness error (maximum deflection), generally measured at the corners that appear as raised edges, and the bowl deformation (bulging/concavity). On the other hand, with these shapes, warpage measurement is limited to deformation in one plane and may be sensitive to bed adhesion parameters. For these reasons, cubic/parallelepiped geometries are sometimes preferred, as they allow multiple analyses of angles and faces, but also require more precise measurement tools for reliable diagnostics (e.g., 3D scanner, tomography), compared to flat rectangular plates.

Generally speaking, it has been reported that warpage grows with increasing length, whereas the effect of width can be negligible for flat rectangular geometries. The influence of part height in cubic/parallelepiped samples is more complex, as a maximum distortion often occurs at intermediate values of part height. This has been ascribed to the extension of thermal stresses to multiple layers due to heat conduction from the last deposited layer, and the occurrence of bending stresses beyond the material yield point [25].

4.1.2 | Cylindrical Disks

Cylindrical disks are particularly effective for analyzing warpage in 3D printing, thanks to their symmetry, which enables nonuniform deformation to be detected immediately [63]. In principle, warpage would occur equally in all directions with respect to the center of the circle, facilitating the identification of isotropic or anisotropic contractions [38]. In addition, the discs are very sensitive at the edges, where warpage usually appears in the form of edge lifting, indicating problems with adhesion to the bed or excessive thermal contraction [63]. Being intrinsically isotropic, the only sources of warpage in cylindrical disks would be ascribed to temperature distribution and evolution. While the central deviation and circular distortion (ovalization) are rather easy to identify and measure, radial twists may sometimes be challenging, with torsion that cannot be straightforwardly detected in the absence of visual cues, and it may also require precise experimental tools.

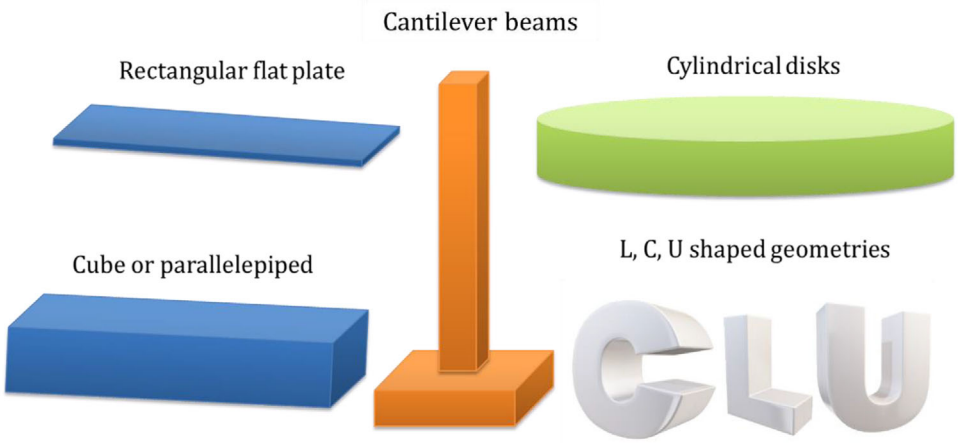

FIGURE 6 | Overview of the different geometries used for ex situ warpage measurements.

TABLE 1 | Main features of the most common geometries used for ex situ analysis of warpage.

Geometry	Limitations	Advantages
Flat rectangular plate	• Deformation measurable only in one plane • Bed adhesion may affect deformation	• Simple design and printing • Easy measurement of warpage
Cube or parallelepiped	• Deformation measurable only in one plane • Need for precise measurement tools	• Simple design and printing • Easy measurement of warpage • The influence of the number of layers and/or thickness can be monitored
Cylindrical disks	• Radial twist (torsion) difficult to monitor	• Immediate recognition of nonuniform deformation • Easy detection of poor adhesion to the bed • Straightforward revealing of severe thermal contraction
Cantilever beams	• Small deformations difficult to be revealed • External factors (e.g., bar weight) may cause bending of the cantilever	• Simple to print • Optimal to measure warpage in long structures • Easy detection of deformation along specific directions: longitudinal deflection (curvature), torsion (end rotation), buckling (out-of-plane deviation)
L-shaped	• Support may be required due to easy lifting at corners and edges	• Easy to print • Analysis of deformation along different axes
C-shaped	• Not simple to print, easy to break at opening	• Analysis of radial and/or circumferential deformation • Measurement of torsional strength
U-shaped	• Distortion caused by bulkiness may arise	• Measurement of deformations over large areas

4.1.3 | Cantilever Beams

On the other extreme, cantilever beams have an asymmetrical structure, with one end fixed and the other one free, and allow direct observation of warpage, particularly at unsupported ends. This geometry makes it easy to measure the deviation of the free end, which can manifest itself as a vertical or lateral deformation from its initial position [56, 64]. In addition, it is possible to detect local deformations near the anchoring point, where stress concentration due to nonuniform contraction may occur during

cooling [56]. Cantilever beams are ideal for analyzing anisotropic contractions, as they reveal how warpage varies along different directions of the structure [15, 16, 63].

Cantilever beams are used to measure warpage in long structures, are simple to print, and allow easy detection of longitudinal deflection (curvature), torsion (end rotation), and buckling (out-of-plane deviation). As drawbacks, small deformations may not be visible to the naked eye, and bending of the cantilever beam may also be caused by external factors, e.g. bar weight.

4.1.4 | L, C, U-Shaped Geometries

L-, C-, and U-shaped geometries play a crucial role in assessing and understanding warpage in 3D printed parts. As shown in Figure 6, L-shaped samples have two perpendicular segments, which allow to analyze deformation along different axes, making it easy to monitor at corners and edges. L-shaped parts are easy to print and analyze, but the risk of lifting at corners and edges may require support. C-shaped geometry is made of a semicircular structure with an opening, needed to analyze radial and circumferential deformation and torsional strength; this allows insights into internal stresses [65, 66], but it is more complex to print compared to L-shaped parts, due to sensitivity to breakage on opening. U-shaped geometry, which combines stability and flexibility, is made of three segments forming a U, for increased stability and stress distribution, to facilitate measurement of strains over large areas, while preventing uplift. This part geometry is used to measure deformations over large areas, as it has a balanced stress distribution, but it can also be bulky and needs to be well aligned on the platform to avoid distortion.

4.2 | In Situ Warpage Measurements

Warpage can also be quantified in real time by directly measuring the strain as it evolves during 3D printing [67–70]. Strain is defined as the deformation per unit length of an object along with a selected direction. Upon temperature change or external load, 3D printed objects undergo mechanical deformation, which can affect the planned geometry. Mechanical strains, if accurately measured, can help to detect warpage of printed objects [71]. The advancement of optical measurement techniques has made it possible to measure strain fields on the surface of objects without contacting them. Therefore, various in situ strain measurement methods have been developed [72, 73].

The main in situ strain measurement techniques used to quantify warpage in 3D printing are listed in Table 2 and detailed in the following paragraphs.

4.2.1 | Digital Image Correlation (DIC)

Digital image correlation (DIC) is an indirect method to monitor strain during the 3D printing process, often adopted thanks to its easy implementation and low-cost setup. In the DIC approach, the surface of the 3D-printed object is speckled with random patterns or textures. Changes in the part geometry can be tracked by using the recorded images captured by a camera or a charge-coupled device (CCD), which can provide detailed information on 2D or 3D displacements. The strain field can be derived from the displacement data obtained from the DIC measurement. 3D-DIC systems offer significant benefits, including low susceptibility to external factors and easy optical configurations [72, 74].

Jani et al. [72] investigated the integration of DIC with infrared thermal imaging for simultaneous real-time monitoring of strain, warpage, and temperature during deposition. The print-head moves out of the camera's field of view for a few seconds after each section of the layer deposition, and such a time range is sufficient to capture the images. This printing method enables the monitoring of defect formation and strain in each layer section as it evolves during the process. The combination of DIC with infrared thermal analysis, used in this specific example for flat rectangular samples with three printed layers, allows for detect immediately the emergence and progression of deformation, thus enabling real-time opportunities to minimize warpage and optimize the process.

Spencer et al. [74] reported that the DIC technique had the potential to be used to monitor residual thermal warpage of printed walls by tracking displacements in the *x*- and *y*- directions, providing an indication of the deformation/warping that occurred during the printing process. Figure 7a,b shows an example of the printed wall with the superposed colormaps of the displacement along x and y directions, respectively. For the *x*-direction (Figure 7a), the base of the wall shows less deformation than the top, due to thermal contraction. Concerning the y-direction (Figure 7b), the center of the wall undergoes minimal deformation, while the right-hand edge reaches maximum displacement. Combining these displacements reveals counterclockwise warpage.

4.2.2 | Strain Gauges

A strain gauge measures the strain on the surface where it is attached. In the context of 3D printing, strain gauges are attached to printed parts or embedded within the polymer matrix, often paired with cost-effective read-out electronics [79] to monitor stress and deformation during the process.

As shown in Figure 8a,b, a strain gauge consists of an electrical resistance that changes when the gauge deforms, causing a measurable variation in the measured voltage. The strain measured by a gauge represents the average strain condition below its surface, caused by 3D-part shrinkage or warping during printing [53, 80].

Jin et al. [80] used strain gauges to detect deformations during MEAM. A plastic film is attached to the printing bed (see Figure 8a), connecting strain gauges to quantify variations in strains caused by residual stress accumulated during printing. The results show that objects printed with a 100% infill density[1] show a continuous increase in the amplitude of the strain (Figure 8c), whereas in the parts obtained with a 50% infill density, the strain does not change significantly over time. It was possible to set a threshold strain value corresponding to a critical deformation to activate a control system, which stops the process or

TABLE 2 | In situ methods for warpage detection during MEAM.

Method	Limitations	Advantages
Digital image correlation (DIC) [74, 75]	• Needs a sensor with a sufficiently high resolution • Noise interference from AM equipment and the camera shutter	• Easy implementation • Low-cost setup
Strain gauges [76, 77]	• The electrical resistance of the material is temperature sensitive; this leads some inaccuracy during measurement. • Local detection of the deformation • Limit number of usages of the same strain gauges	• Easy implementation • Easy connection with the recording device to monitor the stress evolution
Optical interferometry [36, 78]	• Noise interference • Compatibility of the fibers with the high-temperature systems	• Directly transfers stress from the component to the optical fiber • Low sensitivity to the environment. • Simultaneous recording of temperature and stress evolutions

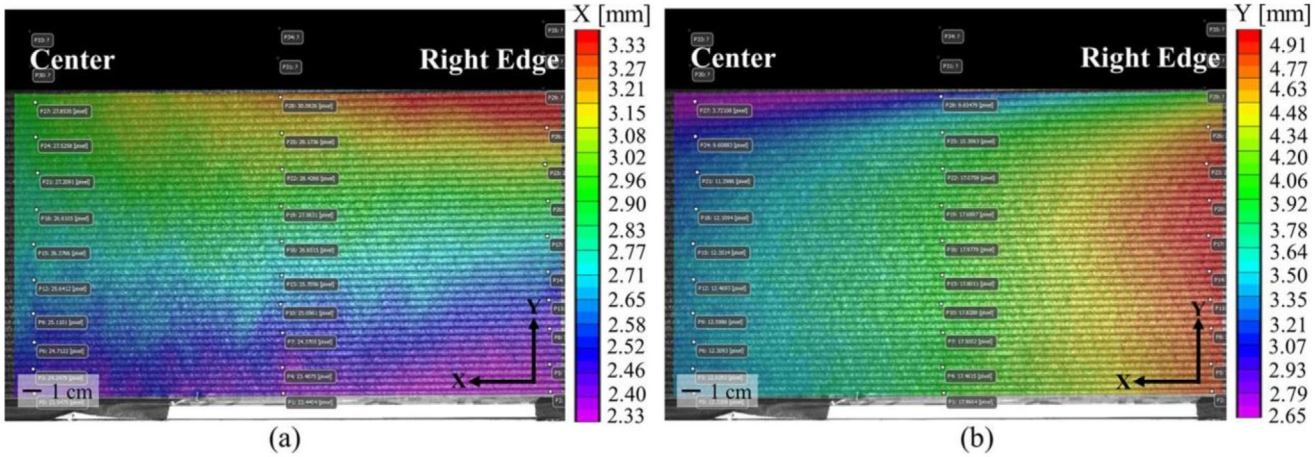

FIGURE 7 | Image of a printed object superposed with a color map of the strain field monitored via DIC for: a) *x*-direction, horizontal displacements, and b) *y*-direction, vertical displacements [74]. Adapted from Ref. [74] with permission from Elsevier. Copyright (2021).

corrects printing conditions to mitigate warpage. Mukhtarkhanov et al. [79] followed part contraction by integrating strain gauges and DIC. Their research revealed that residual stresses due to rapid cooling during MEAM play a significant role in the warpage phenomenon. They found that printing speed and deposition plate temperature are key parameters in limiting these defects.

4.2.3 | Optical Interferometry

Optical interferometry remains a cornerstone technique for assessing warpage and taking appropriate decisions to correct printing conditions. The method is based on several types of optical fibers, such as optical backscatter reflectometry (OBR) [81, 82] or Fiber Bragg grating (FBG) sensor [68, 83]. It is essential for any optical fiber strain sensor to be integrated into the composite material in a manner that allows it to deform in conjunction with the component. Optical fibers are positioned directly within the composite material, interleaved between layers of thermoplastic tapes during the printing process (see Figure 9). This method facilitates the direct transfer of stress from the component to the optical fiber, while the surrounding material serves to shield the fiber–optic sensor from adverse environmental conditions [81]. The OBR delivers a continuous profile of strain, facilitating the detection of manufacturing defects like voids. The analysis of stresses during printing can be combined with the analysis of thermal gradients to select appropriate conditions for limiting the warpage.

Wang et al. [81] incorporated optical fiber sensors directly into the filament, made of short carbon fiber-reinforced polyamide (CF/PA6). The presence of an optical fiber within the printed layers allowed for monitoring strain evolution during deposition and cooling. The optical fibers were included in encapsulation blocks

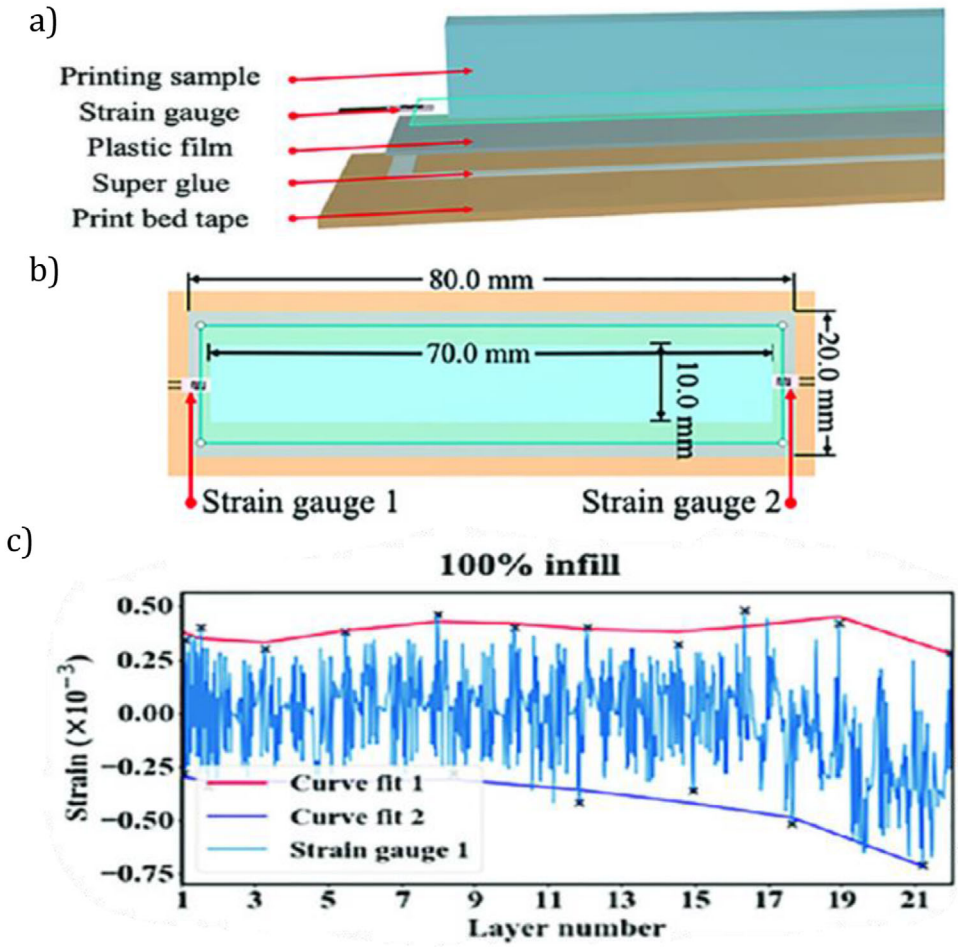

FIGURE 8 | In situ strain gauge measurement for mapping warpage [80], a) Cross-section and exploded view of strain gauge setup; b) Physical dimension of the plastic film and printed sample; c) Example of resulting strain against layer number.

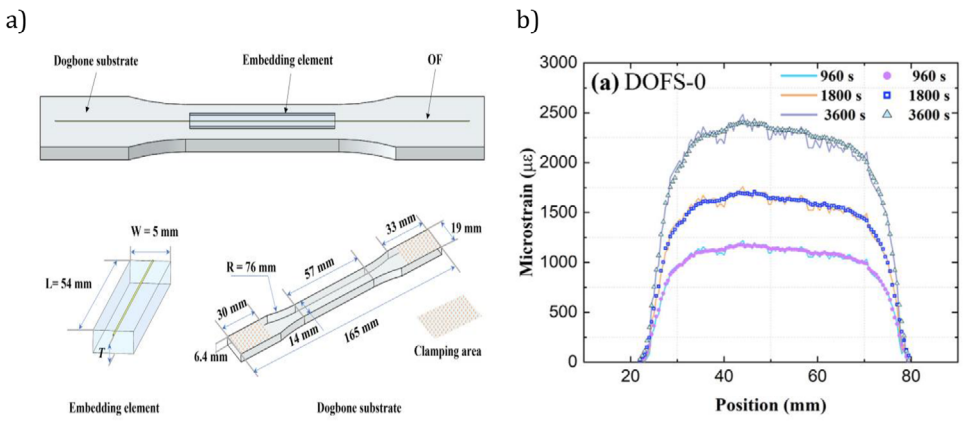

FIGURE 9 | a) The embedding element with optical fiber sensor and the dog bone specimen's geometrical features studied by Wang et al. [81]; b) Comparison of anticipated (line) and measured (markers) relative strains along the implanted distributed optical fiber sensors at three different times.

(see Figure 9a) with varying interlayer thicknesses to examine their influence on strain measurement. This technique revealed uniform stress distribution in the horizontal direction and stress development over printing time (Figure 9b), demonstrating its potential for assessing warpage in 3D-printed parts.

Kantaros et al. [68] studied in situ the stress in a 3D printed object using Fiber Bragg Grating (FBG) sensors to measure residual stress of MEAM parts. Bragg grating sensors (FBG) operate by modulating the refractive index of an optical fiber core through controlled UV exposure, generating a periodic grating. When light

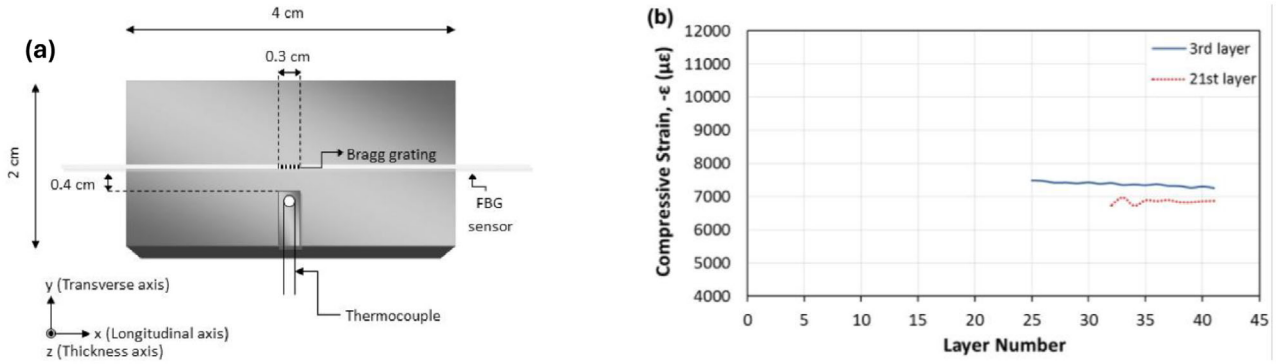

FIGURE 10 | a) Schematic representation of FBG and thermocouple sensors location within the FDM built specimen. b) Strain variations for built specimens: horizontally to the platform for FBG embedded in different layers as a function of printed layer numbers. Reprinted from Ref. [36], Copyright (2016), with permission from Elsevier.

enters the fiber, a particular wavelength (Bragg wavelength, λ_B) is reflected, while the rest is transmitted. The Bragg wavelength is expressed by the following equation:

$$\lambda_{B0} = 2\, n_{\text{eff}}\, \Lambda \tag{1}$$

where:

- λ_{B0} is the Bragg wavelength at a reference state
- n_{eff} is the effective refractive index of the fiber core,
- Λ is the periodic spacing of the grating.

When a fiber is deformed, the periodic spacing (Λ) and effective refractive index (n_{eff}) vary, resulting in a shift in the reflected wavelength. The wavelength shift ($\Delta_{\lambda B}$) is correlated to the deformation (ε) by:

$$\frac{\lambda_{B0} - \lambda_B}{\lambda_{B0}} = \frac{\Delta\lambda_B}{\lambda_{B0}} = (1 - \text{Pe})\,\varepsilon_{\text{res}} \tag{2}$$

where λ_B is the maximum wavelength, and *pe* is the strain-optic coefficient of the fiber, ε_{res} accounts for the residual stress induced by solidification [68].

By monitoring this shift, the FBG sensor can measure strain in real time. If embedded in a material, FBG sensors detect internal strain variations without affecting the structure. The wavelength shift direction indicates whether the strain is tensile or compressive, making FBGs effective for monitoring structural integrity and residual stress in materials. Deformation measured during the process allowed the authors to evaluate the strain of ABS and account for the effect of printing orientation and the layer thickness on deformation.

Kousiatza et al. [36] employed the same technique for measuring the residual deformations in 3D-printed ABS. The sensors were embedded within the printed layers during the fabrication, either longitudinally or transversely, at different depths (3rd, 21st, and 39th layers) (see Figure 10a). The FBG sensors used a grating functioning at a Bragg wavelength of 1550 nm. By analyzing the wavelength shifts, the researchers quantified the residual stress distribution within the specimens. The repeatability of the measurements was verified by embedding FBG sensors at different layers and comparing the strain values obtained across various test conditions. The results obtained from the FBG recordings indicate that the residual strain values generated are significant during the consolidation of the deposited layers of material and are strongly influenced by the position of the samples on the deposition plate.

In conclusion, in situ warpage measurements are crucial for understanding and mitigating deformation issues in 3D printing. Techniques such as Digital image correlation, strain gauges, and optical interferometry provide real-time, noncontact, or embedded monitoring of strain and deformation, enabling the detection of warpage as it occurs. These methods offer valuable insights into the effects of temperature changes, residual stress, and printing parameters on the final geometry of printed objects. By integrating these advanced measurement techniques, manufacturers can optimize printing conditions, reduce defects, and improve the overall quality and reliability of 3D-printed components.

5 | Warpage of Amorphous Polymers

Amorphous polymers are widely used in MEAM [14, 84], also thanks to their reduced warpage, compared to their semicrystalline counterparts. As mentioned above, amorphous polymers have a disordered, glassy structure (see Figure 4) and their processability window and thermo–mechanical properties are mainly defined by the glass transition temperature (*T*g) [14, 64, 85].

The parameters that can influence warpage in amorphous polymers are related to part geometry, material features, and process parameters. The influence of part geometry has been discussed above (paragraph 1 Section 4.1), where details of various geometries of the printed parts are presented and detailed with reference to warpage.

Regarding material features, besides *T*g, the coefficient of thermal expansion and Poisson's ratio need to be considered [25]. More powerful is the set-up of proper processing conditions with a variety of variables that can be optimized, such as nozzle

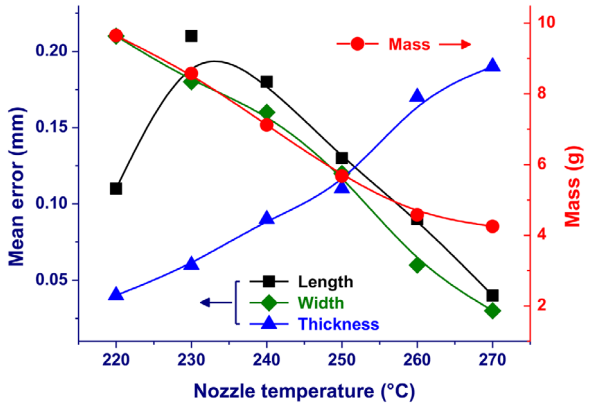

FIGURE 11 | Effect of nozzle temperature on the deviation from prescribed dimension of ABS; the left *y*-axis reports the mean error in length, width, and thickness of dog-bone shaped ABS specimens, whose mass is quantified in the right *y*-axis. Adapted from Ref. [92].

temperature (T_n) [86, 87], deposition plate temperature (T_b) [13, 88] printing speed [86, 87].

The effect of each of these process and materials parameters on the quality of 3D printed parts made of amorphous polymers is detailed below.

5.1 | Effect of Printing Conditions

5.1.1 | Nozzle Temperature

The nozzle temperature directly influences material viscosity; hence, the extrusion process itself. Nozzle temperature also affects adhesion between the layers [5, 64, 85, 88, 89], since at higher temperatures, the polymer viscosity decreases promoting better interdiffusion between layers, thus, better adhesion. This results in an enhancement of the mechanical properties and reduces the risk of delamination and deformation [90]. However, if excessive, the nozzle temperature can cause thermal degradation of the material, weakening its structure. On the other hand, at too low nozzle temperatures, viscosity is too high to allow the polymer to flow properly: this impairs interlayer adhesion and can promote polymer solidification, thus increasing internal stress and the risk of warping. Rivera-Lòpez [91] suggested that low nozzle temperature leads to reduced material flow and lower density of the printed prototype, with a noticeable negative effect on dimensional accuracy. This was also confirmed by Ulkir et al. [92], who quantified the effect of nozzle temperature variation from 220°C to 270°C on the dimensional accuracy of flat dog-bone-shaped ABS samples, by measuring the deviation in length, width, and thickness of the sample, in comparison with the input geometry. A decrease in the mass of the samples of about 56 % was observed between the lowest and highest temperature values, as quantified in the right *y*-axis of Figure 11, which resulted in deviation from the planned geometry of the printed part. As shown in Figure 11, left *y*-axis, higher nozzle temperatures could minimize errors in length and width, but this also resulted in high inaccuracy in thickness. It is worth noting that the increased accuracy in length and with paralleled by the decrease in the mass of the printed specimen.

5.1.2 | Deposition Plate Temperature

The proper selection of the deposition plate temperature is essential for improving the adhesion of the first layer and the management of thermal gradients within the layers [13, 89]. A well-adjusted heated deposition plate reduces the risk of deformation, while a low temperature increases the risk of contraction and detachment of the first layer due to the internal stresses [13].

The optimal adjustment of the deposition plate temperature is linked to the *T*g of the used polymer. Keeping the deposition plate at a temperature close to *T*g allows the part to cool gradually, helping to reduce thermal gradients and internal stresses, thus minimizing warpage [14, 64, 85, 89]. In other words, gradual cooling assures the relaxation of stress and better adhesion of the printed material to the deposition plate [13, 88]. When the deposition plate temperature is below *T*g, the lower layers of the part cool rapidly and become rigid, creating significant thermal gradients with respect to the upper layers. This promotes uneven contractions and increases internal stresses, leading to warping.

Moreover, good adhesion between the first layer and the deposition plate needs to be ensured to minimize the detachment of the part from the plate. The adhesion force depends on the polymer–substrate pair and is also temperature-dependent, being primarily linked to *T*g. For adequate adhesion forces, the deposition plate temperature is generally set at temperatures slightly higher than the *T*g of the printed polymer, as quantified in Figure 12 for two of the most used polymers in FFF, namely PLA and ABS [89].

In the case of PLA (Figure 12a), the adhesion force linearly increases up to the *T*g of 60°C, due to continuously enhanced chain mobility of the polymer [93, 94], whereas above *T*g, an abrupt increase in the adhesion force can be observed, reaching a plateau above 70°C–80°C [95]. In the case of ABS, the adhesion forces increase with temperature and seem to be higher when PI is used as a deposition plate, due to the surface tension of the deposited polymer on the deposition plate [95].

Adhesion between the printed parts and the deposition plate is critical for warpage, because it counterbalances the uneven shrinkage of the layers that tend to detach the part from the printing surface [39]. It has been estimated that the adhesion forces need to be at least 200 N to hold large parts during MEAM [89]. However, too high adhesion forces should also be avoided to prevent damage to the deposition plate during cooling. In other words, the deposition plate temperature needs to be optimized to attain a moderate adhesion force range: for instance, based on the data shown in Figure 12, for the PLA/glass pair, the deposition plate temperatures should be between 80°C and 120°C [89]. Removal from the deposition plate after MEAM may also damage both the printed part and the substrate, and ideal temperatures to avoid surface damage imply adhesion forces close to zero [89].

5.1.3 | Layer Height, Printing Speed, and Infill Density

The number of layers required to create an object determines the printing speed and, thus the printing time required. The thinner the layer thickness, the longer it takes to make a 3D printed object of a given height. Thinner layers in general improve the quality of

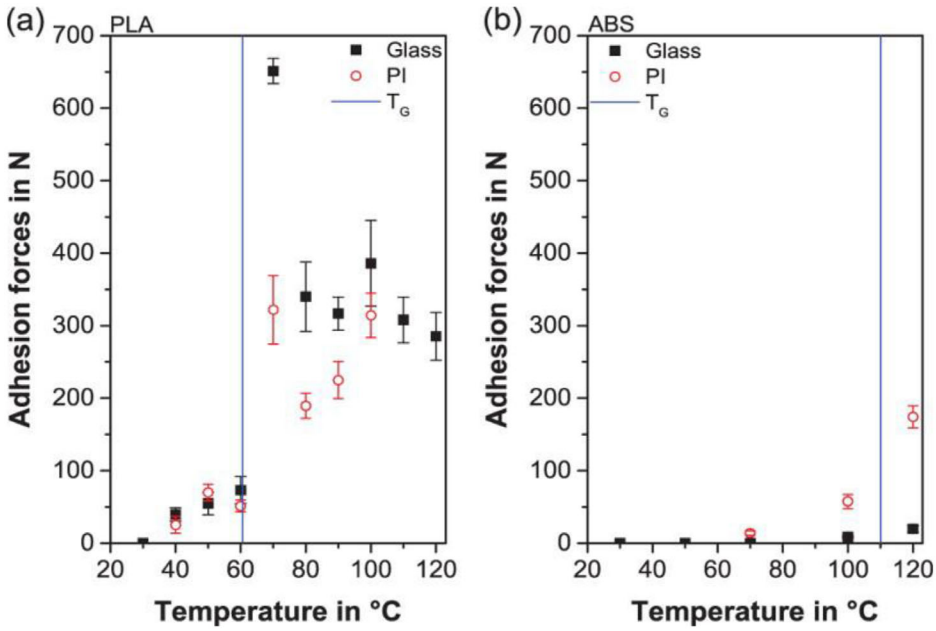

FIGURE 12 | Adhesion forces as a function of deposition plate temperature for PLA (a) and ABS (b) on glass or PI; The *T*g of the two polymers (60°C and 110°C, respectively) is drawn as blue vertical lines. [89].

the printed part, leading to a smoother surface and more accurate details visible in the *Z*-direction (height) of the model, but at the same time, thin layers cool rapidly, because of their small mass and high surface-to-mass ratio, which increases internal stresses, hence the risk of warping. However, too thick layers may cool unevenly, with the formation of thermal gradients that also affect internal stress and warpage [96]. Combined simulation models and experiments conducted using ABS to print a flat rectangular part showed that increasing layer thickness also has a moderate effect on warpage, because a larger volume of material is subjected to shrinkage during the thermal transient following the deposition of a new layer [25].

The printing speed is the rate at which the printer head moves along the *X*–*Y* plane. Combined with layer thickness and with the nozzle-to-bed distance, printing speed impacts the thermal history of the printed component, including the cooling rate of each layer, which affects the strength of the bonds between layers and residual tensions, hence affecting warpage [97]. Printing speed can be optimized to minimize warpage, as too low or too high speed can increase warpage deformation [97]

Infill density refers to the amount of material that is used to fill the internal space of the 3D-printed parts. Increasing the infill density can improve the strength and rigidity of the printed object, but it also increases the time and cost required to print the object. This parameter is strictly related to the infill pattern, which determines the shape and the structure of the infill material within the printing orientation object. Common infill patterns include grid/linear, triangular, honeycomb, and trihexagonal [98], with additional parameters that need to be set that comprise raster width and angle: raster width indicates the width of deposition layer, which is directly linked to the nozzle diameter, whereas the raster orientation (or angle) is the deposition path (or angle) along the *x*-axis of the MEAM building stage [99]. The deposition path is one of the main factors affecting part warping and anisotropy, because the deposited layers have an elliptical cylinder morphology, hence voids are generated in a printed structure when the layers stack together [100].

Both infill pattern and density influence anisotropy and temperature distribution within the printed part, and their optimization is strictly related to the overall shape of the printed part [101]. With 100 % infill density, numerous voids can be generated between deposited layers, which makes the thermal expansion coefficient of the specimens highly anisotropic [100]. Moreover, the raster orientation affects the temperature distribution in the material, resulting in local reheating of the already cooled deposited layers. When a linear (90°/90°) raster pattern is used, high thermal shrinkage along the longitudinal direction is generally observed [100], with warpage that can be reduced using a zigzag (45°/45) pattern, which also allows more uniform stress distribution.

5.2 | Effect of Material Features

The main material features that affect warpage in amorphous polymers are *T*g and the thermal expansion coefficient (CTE), and both define process parameters, as detailed above. The coefficient of thermal expansion, defined as the change in unit length per degree of temperature change, is strictly related to thermal deformation, as well as to the induced residual stresses and strains in the produced MEAM parts, hence of key importance in mitigating warpage.

Despite being one of most used polymers in MEAM, ABS has a high CTE, which causes shrinkage and warpage of printed parts [24]. To overcome these drawbacks, ABS is often blended with other polymers that have lower CTE. One typical example is blends of ABS with thermoplastic polyurethane (TPU): not

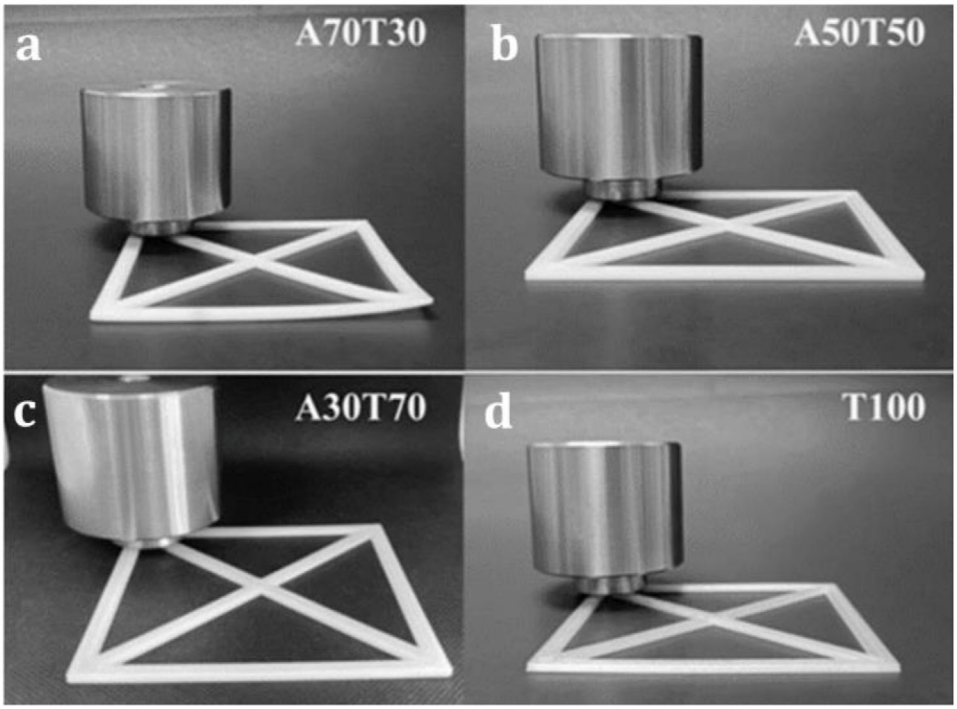

FIGURE 13 | Warpage deformation of: ABS/TPU blends with different compositions. Adapted from [103].

only TPU have a lower coefficient of thermal expansion, but it also requires lower extrusion temperatures compared to ABS, which results in reduced internal stresses upon cooling [102]. Experimental tests proved that blending with TPU is an efficient strategy to reduce warpage in ABS printed parts [103], as shown in Figure 13 that compares warpage in ABS/TPE blends with different compositions, with the neat ABS filament that could not be printed under the chosen processing settings: a sizable warping deformation can be noticed in the blend made with 70% ABS and 30% TPU (A70T30), which is practically eliminated when larger amounts of TPU in the A50T50 (50% TPU) or A30T70 (70% TPU) are added in the formulation. Besides the lower CTE, the favorable effect of TPU on reduction of warpage of ABS printed parts is also due to the good intermolecular diffusion between ABS and TPU layers [104], favored by the hydrogen bonds between the blend components [105]. Conversely, when ABS is blended with a polymer with higher CTE, the warpage worsens. This is the case of blends with PETG, where increasing amounts of PETG were found to lead to more sizable warping deformation in ABS/PETG blends [106].

One of the most common methods to reduce residual deformation is to add fillers that improve thermal conductivity and reduce the coefficient of thermal expansion. The most used filler to tailor thermal conductivity and CTE in amorphous polymers for MEAM is carbon fibers [107–109]. Of special interest are negative thermal expansion materials (NTE) that exhibit elastic volume contraction with the increase of temperature, contrary to ordinary materials that show elastic volume contraction as the temperature decreases. A NTE filler, namely $Zn_{1.6}Mg_{0.4}P_2O_7$, has been recently tested with success for FFF of ABS, with warpage of a 100 mm × 5 mm × 2 mm bar-like test piece that was reduced by about 75% with the addition of 40% of filler, compared to the neat material [110].

6 | Warpage of Semicrystalline Polymers

In addition to the effects detailed for amorphous polymers, the warping of semicrystalline polymers in MEAM is further complicated by the dimensional alterations induced by crystal formation during and after layer deposition, mainly including thermal stress, chain orientation, and density variations. Crystallinity, crystallization kinetics, crystal polymorphism, and morphology are crucial in this process, as they influence the distribution of amorphous and crystalline phases, as well as the residual stresses in the material. Therefore, the analysis of these parameters is a key issue for understanding and controlling warping.

Crystallization often causes a variation in material dimension, most often shrinkage (see Figure 5), since crystals generally have a higher density compared to the amorphous material. The shrinkage occurring upon crystallization, which adds to the shrinkage caused by the decreased temperature upon filament deposition, can be significant, as quantified in Table 3, which compares crystal density data of a few representative polymers, and may cause warpage and part distortion. For a given polymer, density can vary depending on the specific crystal modification that develops. A typical example is isotactic polypropylene, where the crystal density increases from 0.8665 g cm^{-3} of the amorphous material to 0.9405 g cm^{-3} upon crystallization in α-modification, and this leads to a decreased volume of about 8 %; a lower shrinkage instead takes place when the polymer develops β-crystals, whose density is 0.921 g cm^{-3}, hence chain packing in β-form results in a decrease volume of 6%, lower than that of crystallization in α-modification. Since crystal polymorphism largely affects polymer properties [113, 114], MEAM process may need to be tailored to attain a specific crystal modification, as for instance, electroactive β-crystals in poly(vinylidene fluoride) (PVDF), to fabricate energy harvesting structures [113].

TABLE 3 | Crystal density of main semicrystalline polymers used or studied in MEAM.

Polymer	Density (g cm^{-3})					Refs.
	Amorphous	Crystal form—density				
PE	0.855	I – 1.00	II – 0.98	—	—	[114]
PP	0.8665	α – 0.9405	β – 0.921	γ – 0.938	Mesophase – 0.920	[115, 116]
PB	0.868	I – 0.95	II – 0.907	—	—	[115]
P4MP1	0.838	0.828	—	—	—	[114]
PLA	1.245	α – 1.285	β – 1.301	—	—	[117]
PET	1.335	1.445	—	—	—	[118, 119]
PA-6	1.100	α – 1.23	γ –1.16		—	[120–123]
PA-12	0.990	α –1.034	γ –1.085		—	[124]
PVDF	1.68	α –1.92	β –1.97			[125]

6.1 | Effect of Printing Conditions

To mitigate warpage, proper control of crystallization kinetics, or even suppression of crystallization, can be crucial: the intrinsic shrinkage caused by cooling that adds to the volume contraction linked to the phase transition can also cause uneven cooling, due to latent heat evolved during crystallization, create internal stresses, and contribute to dimensional and geometrical inaccuracy. Moreover, the printing conditions may play a crucial role in crystal polymorphism, and the developed crystal modification can strongly affect shrinkage and warpage, as discussed above (see Table 3). The following paragraphs present an overview of the specific effects of each MEAM parameter that can be adjusted to tailor crystal formation in the printed part, and in turn, mitigate warpage.

6.1.1 | Nozzle Temperature

Processing temperature, from the liquefier to the nozzle, must be high enough to melt the semicrystalline material and allow it to flow, to avoid nozzle obstruction. As also noted for amorphous polymers (paragraph 4), if the nozzle temperature is too low, the material may not flow or melt properly and may also display poor adhesion between the layers and uneven crystallization [126]. Conversely, a too high nozzle temperature can degrade the material, a critical issue for polymers susceptible to thermal degradation, like PLA. It can also result in cooling too fast, once the material exits the nozzle, which can also cause uneven crystallization that increases warpage [126].

An optimization of the extrusion temperature and extrusion rate (the main processing parameters linked to polymer melting kinetics) was recently presented for PLA [127]. Experimental analyses of the thermal properties of the printed parts, combined with modeling and simulation of flow and temperature fields inside the liquefier to account for the filament melting, were employed to map the temperature profile that determines crystal formation in the printed layers, and in turn, layer adhesion, part distortion, and warpage. Cadete et al. also investigated the effect of extrusion temperature on the crystallinity of 3D printed PLA [128]. The results showed that at higher nozzle temperatures, crystallization in the printed parts is promoted, whereas at low nozzle temperatures may compromise solidification. Conversely, the opposite trend was observed when samples were printed using high nozzle and deposition plate temperatures, where larger crystallites were achieved. This is linked to the long time spent by the macromolecules in the temperature range of crystallization, when higher nozzle and deposition plate temperatures are used [129].

The influence of the nozzle temperature on crystallization upon MEAM was studied for other polymers. For isotactic polypropylene (PP), Wang et al. compared two different nozzle temperatures (200°C and 250°C) as a tool to tailor crystallization kinetics and, in turn, crystal polymorphism. The extrusion temperature determined the crystallization temperature, and in turn, crystal polymorphism, because growth of β-crystals is favored at crystallization temperatures between 100°C and 140°C [130]. The use of a nozzle temperature of 200°C resulted in crystallization in the temperature range where β-crystals are favored; hence, a large number of β-crystals developed in the sample processed at a lower temperature. Conversely, when the nozzle temperature was set at 250°C, maintaining the same deposition plate setting, crystallization occurred at higher temperatures, and a smaller fraction of β-crystals was produced. The different decrease in volume attained by crystallization in the two crystal modifications (see Table 3) affects material shrinkage upon cooling, and therefore warpage. This adds to the lower modulus and yielding strength imparted by the presence of β- crystals, compared to α-form, so when the nozzle temperature is 200°C, the printing part is weaker with respect to the same part obtained at 250°C [131].

6.1.2 | Effect of Deposition Plate Temperature

The influence of nozzle temperature on crystallization kinetics and part warpage is often analyzed together with deposition plate temperature, because the first layer is deposited onto a heated print substrate, which affects the cooling rate, and in turn crystallization kinetics. The effective cooling rate of the filament is determined by a combination of the nozzle temperature, the

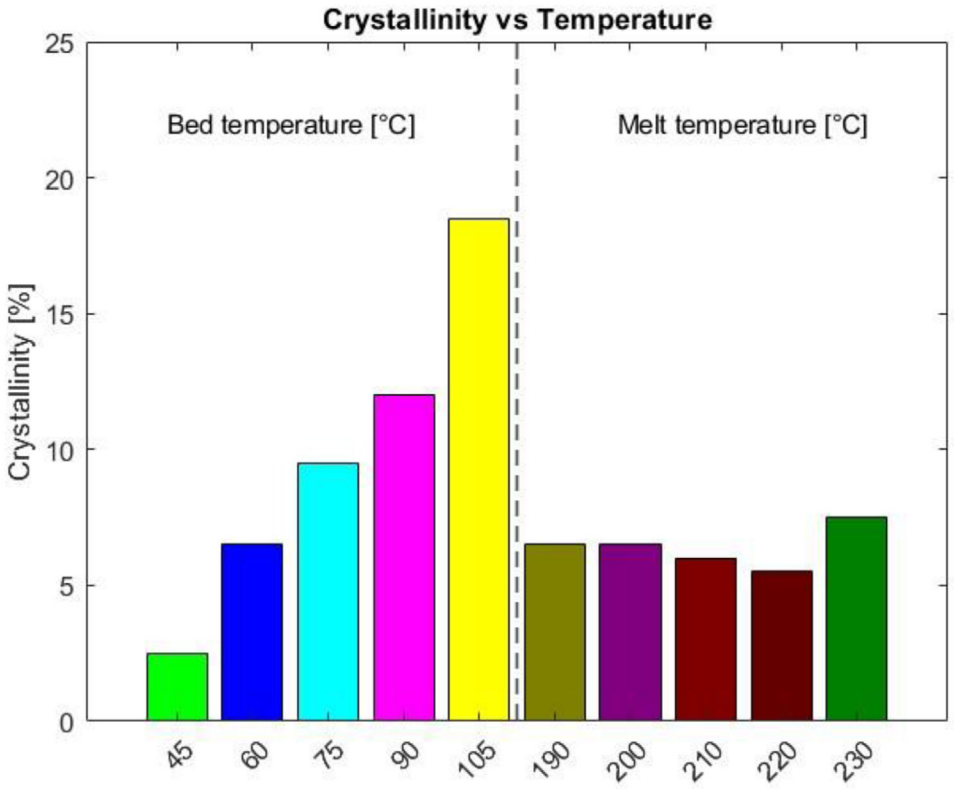

FIGURE 14 | Crystallinity degrees for PLLA printed with different deposition plates (or bed) (left) and nozzle temperatures(right). [132].

deposition plate temperature, the chamber temperature, and the layer height. The effect of both extrusion and deposition plate temperatures on crystallinity of PLA parts was investigated by Benwood et al., who quantified a significant increase in crystallinity from 2 to 18 % upon variation of the plate temperature from 45°C to 105°C, as shown in Figure 14 [132]. Conversely, a variation of nozzle temperature in the range 190°C–230°C did not lead to a sizable variation in crystallinity, as illustrated in Figure 6, however, an increase in printing temperature affected dimensional stability: the samples began to warp and had difficulty in adhering to the deposition substrate [132].

The effectiveness of proper setting of the deposition plate temperature as a process parameter to enhance crystallinity is due not only to the different crystallization kinetics at the substrate temperature, but also to the varied cooling rate upon filament deposition, which affects both crystallization and mechanical properties [33, 111, 131, 135–137]. Every time the print head passes and moves away, the printed layer undergoes cyclic temperature fluctuations, which favor crystal nucleation and the formation of smaller crystals and thus enhance mechanical properties [132].

As exemplified above for PP, the printing condition can affect crystal polymorphism, which determines material shrinkage upon filament deposition and leads part warpage. This was also observed for PLA, whose crystal polymorphism is set by the crystallization temperature: α-form predominates at temperatures of 120°C or higher, whereas at lower temperatures, generally attained using low deposition plate temperatures, leading to fast cooling, the conformationally disordered α'-modification prevails [138, 139]. The deposition plate temperature can influence crystallization of PLA, in α'- or α-form, which in turn affects void formation between deposited layers and thus the mechanical performance and warping, as quantified in [138].

Ju et al. found a strong influence of deposition plate temperature on the warpage of PP block copolymers with ethylene [8]. The chosen processing parameters allowed crystallization of the copolymers into both α- and γ-forms, but proper regulation of both T_b and T_n allowed to tailor the α-/γ-crystals ratio, without a sizable change in the overall crystallinity, which had a marked effect on part warpage. It was found that a higher content of γ-crystals resulted in less pronounced warpage at parity of crystallinity, as shown in Figure 15, probing a close correlation between the content of γ-crystal and part deformation of MEAM-printed iPP. The effect is not linked to the crystal density, because the two polymorphs have similar density (see Table 3), but to the higher rigidity of γ-crystal, which significantly reduces the volume shrinkage of PP during layer deposition [8].

The combined effect of nozzle and deposition plate temperatures was also analyzed for PEEK, a polymer with very high melting point, whose MEAM requires high temperature of processing: PEEK is generally printed using nozzle temperatures of 350°C – 440°C, deposition plate temperatures of 100°C–150°C, and chamber temperatures of 90°C – 160°C [139]. The high processing temperatures, coupled with PEEK's fast crystallization, generally cause high thermal stress, unevenly distributed between printed layers, and can result in thermal cracks, poor interlayer adhesion in the 3D printed parts, and part warpage [140]. Optimized nozzle and deposition plate temperatures able to reduce thermal gradients, strengthen interlayer bonds, and

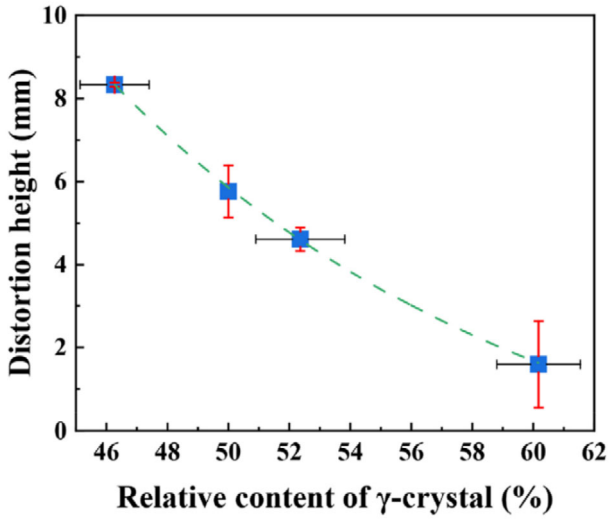

FIGURE 15 | The height warpage (mm) as a function of the relative content of γ-crystals in samples printed at different bed temperatures. Reprinted with permission from Ref. [8].

minimize warpage in PEEK were identified as 380°C and 140°C, respectively [141].

6.1.3 | Printing Speed and Layer Height

Similar to amorphous polymers (Section 5), printing speed and layer height can affect warpage in semicrystalline polymers, with additional contributions arising from the varied cooling rate that affects the crystallization rate [33]. The influence of these parameters on warpage can be more consistent than other conditions, like chamber and nozzle temperature, as demonstrated for PEEK [142].

Polymers are generally characterized by poor heat transfer properties, so a thermal gradient is present across the layers, leading to anisotropy and inhomogeneous thermal history in the whole printed sample and resulting in nonuniform degree of crystallinity. A printing speed that is too low leads to long printing times: the sample is exposed to heat for a longer time, which can promote macromolecular diffusion [131]. On the other hand, high printing speed may result in over-extrusion on the product edges or under-extrusion in other parts.

Uneven crystal formation caused by varied printing speed upon printing was probed by Nogales et al.: a Π-shaped sample was printed on a movable build plate, and microstructure development was studied by simultaneous small- and wide-angle X-ray scattering (SAXS and WAXS, respectively) [143]. In the parts of the sample where the printing head changes its direction, like corners and edges, the printing speed is reduced, and this affects the local temperature, and in turn, crystal formation.

The printing speed also influences the residual alignment and orientation of polymer chains in the extrusion direction, and in turn crystallization, due to the pressure drop in the nozzle, as demonstrated by Costanzo et al. upon analysis of the residual orientation in printing PLA parts [2]. A way to reduce the chain orientation is to use a lower printing speed, higher nozzle temperature, and higher deposition plate temperature. Slower printing speed determines a long total printing time, which, combined with high deposition plate temperature, can induce crystal annealing/perfection and chain relaxation, because the prolonged exposure of the just printed parts to the high temperature nozzle favors diffusion and chain rearrangements, and in turn loss of the residual orientation/stresses, which can mitigate part warpage [96].

Layer height parallels the combined effects of nozzle and deposition plate temperatures (which determine the effective cooling rate) on the residual orientation of the chains and crystallinity: a thin printing layer corresponds to fast deposition on the deposition plate, and limited time for chain rearrangements, leading to high orientation and low degree of crystallinity [138]. Moreover, the infill density or porosity of the printed samples may also influence the phenomenon: internal stresses that cause warping may arise from high infill densities, and the use of less dense infill patterns can help reduce such stresses [96]. Wang et al. showed that for PLA, low layer height combined with high deposition plate temperature allows to obtain smaller voids in the printed part, due to the shorter distance between centers of two adjacent layers. In addition, thin layers correspond to a long time needed to print the final product, and this might imply that parts with thinner layers stay longer in the melting temperature range, which helps the interfacial diffusion [129].

6.2 | Effect of Modification of Material Properties: Copolymers, Blends, and Additives

To control crystallization in semicrystalline polymers as a tool to mitigate warpage, other strategies that add to the optimization of processing parameters can be followed; the most common ones comprise modification of material composition via copolymerization, blending, or formulation with specific additives.

6.2.1 | Copolymerization

This involves the incorporation of different monomers into the polymer chain: the comonomers can influence the crystallization behavior, being either included or excluded from the crystal lattice [12, 144–147]. Overall, the influence of copolymerization on crystallization behavior depends on the nature, content, and chain distribution of the comonomer [147].

A few cases of the influence of copolymerization on MEAM process have been mentioned above, e.g., PP block copolymers with ethylene, which have excellent printability: the comonomer lowers the crystallization rate, and also affects crystal structure and morphology, allowing for obtaining a low level of shrinkage and warpage in the printed part [12].

Several authors have investigated PP copolymers for MEAM. Spiegel et al. synthesized copolymers of isotactic polypropylene with 1-butene and 1-hexene, to explore their potential as feedstock materials for the 3D printing process. The copolymerization of PP with these monomers led to a decrease in the degree of crystallinity of the polymer as the monomer content increased, since these large comonomers act as constitutional defects disturbing the regular arrangement of PP chains. This reduction in

crystallinity could improve printability by minimizing shrinkage during cooling, thereby reducing warpage [148].

Polyesters are normally copolymerized to tailor crystallization kinetics and improve their printability. A typical example is poly(ethyleneterephtalate)-glycol (PETG), a glycol-modified PET, where copolymerization with glycol units prevents crystallization [149], leading to 3D printed parts showig good chemical resistance and mechanical performance [150]: this made PETG one of the most currently used materials in MEAM [151]. Also, the higher analogue of PET, poly (trimetylene terephthalate) (PTT), can be easily modified to improve printability. In PTT copolyesters containing isophthalate-co-sebacate units (PTTIS), the major impact of sebacate units on crystallization was reported, and a composition optimized for MEAM was suggested as made of terephthalic/isophtalic ratio of 7/3 and 1.0–3.8 mol% of sebacate [151].

Polyetheretherketone (PEEK) is also widely used in MEAM for its outstanding properties, despite the fast crystallization that restricts its use 152–156]. Copolymerization of PEEK has been explored as a tool to mitigate crystal formation and warpage, to attain initially amorphous 3D printed parts, followed by post-processing crystallization to improve mechanical properties [156, 157].

6.2.2 | Polymer Blends

The addition of a second polymer is another tool to manipulate crystallization kinetics and crystallinity, which can either be facilitated or hindered by blending. Crystal nucleation can be favored by blending, via migration of nucleating heterogeneities from one component to the other [139, 158], or in polymer pairs that crystallize in different temperature ranges [157], or, in the case of immiscible blends, when the phase separation boundaries can act as nucleation sites [158].

The effect of blending on the crystal growth rate (G) is more complex, as it largely depends on the miscibility of the polymer pair and can either favor or hinder crystallization [159]. In miscible polymer pairs, G is a complex function of several parameters, including molar mass, composition, as well as glass transition and melting temperatures of the blended components. Most commonly, blending decreases the crystal growth rate, due to dilution of the crystallizable polymer, and only in a few cases of the enhanced crystal growth rate has been reported, when the second polymer acts as a plasticizer, favoring chain mobility [159].

In partially miscible or immiscible blends, the non-crystallizable component, segregated as a dispersed phase, must be rejected and/or occluded by the growing spherulites. This generally affects spherulite growth, with a decreased phase transition kinetics, although a few cases where the addition of an immiscible polymer has a negligible effect on crystallization rate have been reported as well [159].

Fast crystallization kinetics limit the interfacial adhesion between the printed layers and produce internal stress and deformation. Ho et al. [160] improved the adhesion of printed polypropylene by blending it with a polyolefin elastomer. They blended 20–40 wt.% of an elastomeric poly(ethylene-*co*-octene) copolymer (EOC) with PP to enhance the mass flow rate upon the extrusion process, interlayer adhesion, and mitigate warpage.

Zander et al. used blends of both recycled PP and PET, and PP and PS, as feedstock for 3D printing. Blending PP with rigid polymers like PS and PET, plus a compatibilizer, led to a reduction of crystallinity, which allowed them to produce flexible filament made of recycled PP/PET and PP/PS blends, with good printability and reduced warpage [161].

Blends of polyethylene (PE) have also been attempted to overcome the limits due to the high crystallization rate and the significant reduction of volume that takes place during cooling. Blending PE with poly(ethylene-*co*-vinyl acetate) copolymer (EVA) not only allows for a decrease in the degree of crystallinity of PE, but it can also affect chain flexibility, decreasing the warpage of printed parts [162].

Blending with an amorphous polymer has been exploited as a strategy to reduce crystallinity, also in MEAM of polyamides. Jia et al. developed a polyamide-6 (PA6) based filament containing, as an amorphous polymer, a maleic anhydride grafted poly(ethylene 1-octene) (POE-*g*-MAH) [163]. The amorphous polymer disturbs the crystallization of PA6, due to its short-chain branches that hinder the orderly and regular arrangement of PA6 chains; this results in a decrease of internal stress and thus of shrinkage and warpage in the printed parts. Further reduction of shrinkage and sizably enhanced shape stability can be attained with ternary blends, where atactic polystyrene (15–20 wt.%) has been added to a PA6/POE-*g*-MAH 60/40 blend [163]. Also, blending with acrylonitrile-butadiene styrene (ABS) has been proven to be effective in reducing, or even eliminating, warpage in PA6 printed parts, to attain products with high physical and mechanical properties, such as high tensile strength and Young's modulus [164].

6.2.3 | Additives

Additives are materials added in small amounts to a polymer formulation to modify its properties, enhance its performance, or improve its processability, and can also affect polymer crystallization. Nucleating agents are purposely added molecules able to lower the surface energy barrier towards nucleation, thus promoting the simultaneous growth of a high number of tiny crystals at higher temperatures upon cooling [165]. Plasticizers can also fine tune crystal growth, by enhancing chain mobility. Both the smaller crystal size attained by the addition of nucleating agents and the higher chain flexibility imparted by formulation with plasticizers generally have a positive impact on the mechanical performance of the material and can also affect the layer-by-layer deposition process in MEAM. Moreover, both types of additives can influence crystal polymorphism, with the effect on warpage discussed above. Spoerk et al. [39] found that filled polypropylene composite (with filler having 30 μm average dimension and loading of 30% vol) greatly decreases warpage and shrinkage, and improves mechanical performance. Fillers in micro- and nano-composites that are also specifically

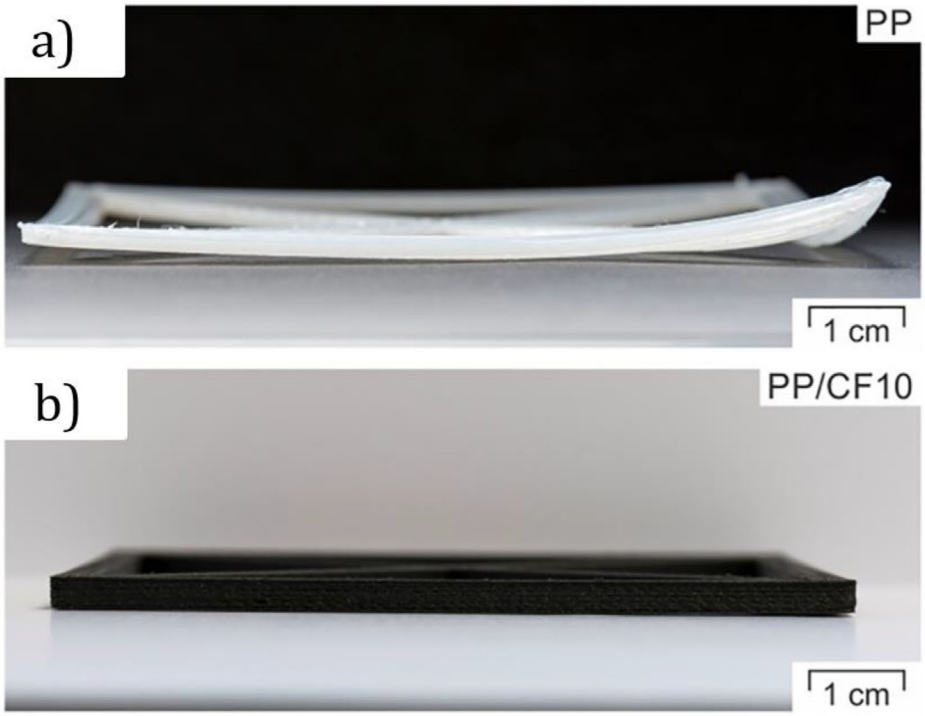

FIGURE 16 | Warpage of 3D-printed specimens, for a) PP and b) PP filled with 10 wt.% carbon fiber [22].

used in MEAM to mitigate warpage can also affect crystallization kinetics [166, 167]. Small-sized fillers generally favor the reduction of warpage and shrinkage, while at the same time imparting improved mechanical properties, also thanks to their efficiency as nucleating agents [168 169, 170].

Glass fibers have been shown to provide an evident improvement in printability and mechanical performance in several polymers like PP, PLA, or polyamides [171–175]. A sizable decrease in warpage and a high dimensional accuracy are obtained in PP reinforced with glass fibers, with respect to the neat material [170].

Carbon fibers are also commonly used to enhance the properties of filaments for MEAM and improve printability and dimensional accuracy of the printed parts, as reported for PLA [176–178], polyamides [179–181], PP [179, 180], or PEEK [179]. Spoerk et al. [22] reported that the incorporation of 10 weight % carbon fibers (CF 10) into polypropylene significantly enhances its thermal conductivity. This improved heat transfer resulted in a more uniform temperature distribution within the printed specimens, leading to a reduction in internal and residual stresses. Consequently, the material exhibits better dimensional accuracy compared to neat PP [Figure 16], despite the high aspect ratio of the fillers.

Metal powders have been added as fillers in polyamides to fabricate filaments, like aluminum or iron powder, which are effective additives for improving the 3D printing properties of polyamide matrices, by reducing the coefficient of thermal expansion, with a consequent reduction of the distortion and warpage of the samples [182, 183].

7 | Modeling of Warpage

MEAM is a highly complex process that involves controlling all print-related parameters and a range of thermal, physical, and mechanical properties, making trial and error an ineffective method of ensuring flawless parts [184, 185]. Process simulation is the best practice to assess warpage prior to printing [41, 42]. Numerical models were developed to describe the evolution of stress leading to deformation and warpage in polymeric parts. Simulation with a finite element analysis (FEA) can be used to predict deformation during the process, also in the case of MEAM [186, 187].

One of the first models adopted for the injection molding process was proposed by Jansen et al. [186], who evaluated shrinkage and deformation occurring during solidification through a force balance. In that model, the material can shrink due to density changes and also by the effect of pressure and crystallization. The model was applied to a thin slab obtained with the injection molding process: the material is injected into a cavity with a rectangular shape where it cools and solidifies. Figure 17 shows a sketch of the slab and the confining cavity, where the melt advancement occurs along the x direction. It can be seen that the material solidifies from the external walls toward the center.

Slab is symmetric, thus the thickness of the solid layer (z_s in the sketch) is the same in the upper and bottom part. The molten core thickness, which cools more slowly than the outside, is equal to $2(D - z_s)$. The temperature distribution along the width direction (y direction) is assumed to be homogeneous; pressure distribution is homogeneous along both y and z directions. The material can be assumed to shrink uniformly, and its deformation depends

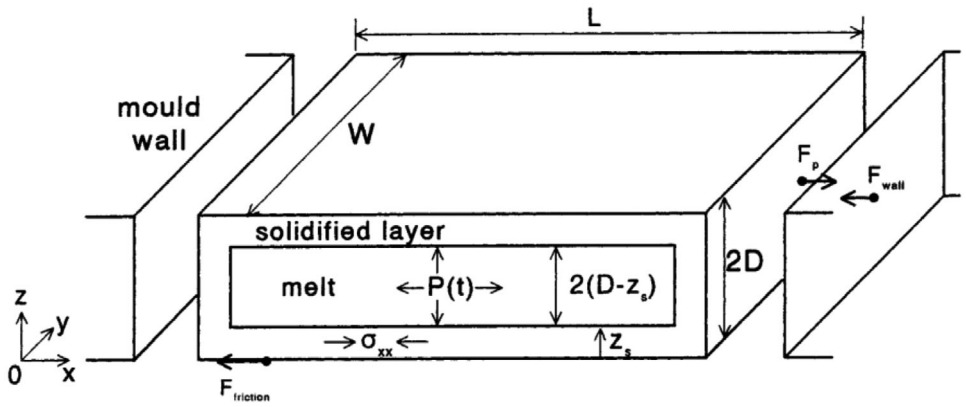

FIGURE 17 | Schematic view of the constrained solidifying slab [186].

on the stress evolution. Since during the injection, temperature is assumed to be uniform along x direction by the effect of the fountain flow, the shrinkage must start only when the cavity is filled with the molten polymer. If the material shrinks, each point of the material domain does not retain its reference position. The strain is the local displacement of a dash with respect to its reference state. The strain components are given below:

$$\varepsilon_{ii} \equiv \frac{\partial u_i}{\partial x_i} \cong \frac{\Delta x_i - \Delta x_i^o}{\Delta x_i^o} \; i = x,\; y,\; z \tag{3}$$

The strain component ε_{ii}, can be interpreted as the local relative displacement of a small dash, with length Δx_i^o at its reference state. The displacements can be seen as the integral of the strain components, starting from a fixed point. The displacement is the main cause of the stress accumulation in the material.

The total tensile mechanical stress can be expressed as follows:

$$\sigma_{xx}\;(x,\;y,\;z,\;t) = -P\,(x,\;y,\;t) + s_{xx}\,(x,\;y,\;z,\;t) \tag{4}$$

$$\sigma_{yy}\;(x,\;y,\;z,\;t) = -P\,(x,\;y,\;t) + s_{yy}\,(x,\;y,\;z,\;t) \tag{5}$$

$$\sigma_{zz}\;(x,\;y,\;z,\;t) = -P\,(x,\;y,\;t) \tag{6}$$

σ denotes the stress, P the pressure. The stress along the thickness does not depend on z. The stress components s_{ii} are related to the strain in the solid, following Hooke's law [187]:

$$s_{xx}\;(x,\;y,\;z,\;t) = \frac{E}{1-\nu^2}\;\left[\varepsilon_{xx} + \nu\varepsilon_{yy}\right] - \frac{E}{1-\nu}\,\epsilon^j \tag{7}$$

$$s_{yy}\;(x,\;y,\;z,\;t) = \frac{E}{1-\nu^2}\;\left[\varepsilon_{yy} + \nu\varepsilon_{xx}\right] - \frac{E}{1-\nu}\,\epsilon^j \tag{8}$$

E is the elastic modulus, ν is the Poisson' coefficient. ε^j is the isotropic shrinkage that can be due to thermal contraction/expansion, ε^T, crystallization ε^c, or pressure effect. It can be assumed that the expansion (and the corresponding stretching forces) is defined as positive, and shrinkage (and compression forces) as negative. During part solidification, crystallization may occur inducing additional decrease in volume, consequently, changes in $\varepsilon^T$and ε^c tend to be negative (shrinkage).

$$\epsilon_{ii}^T\;(x,\;y,\;z,\;t) = \int_{T_s}^{T} \alpha dT \cong \alpha\left[T\,(x,\;y,\;z,\;t) - T_s\right] < 0\; i = x,\; y,\; z \tag{9}$$

$$\epsilon_{ii}^c\;(x,\;y,\;z,\;t) = -\int_{\xi_s}^{\xi} C_{cr} d\xi \cong -C_{cr}\left[\xi\,(x,\;y,\;z,\;t) - \xi_s\right] < 0\; C_{cr} \cong \frac{\rho_{cr} - \rho_{am}}{3\rho_{am}} \tag{10}$$

$$\epsilon^p = -\beta P\,(x,\;y,\;t) \tag{11}$$

α is the linear thermal expansion coefficient, ξ as the degree of crystallinity, C_{cr} as the linear shrinkage from an amorphous to 100% relative crystalline degree. T_s and ξ_s are the values of T and ξ at the solidification; β is the linear compressibility.

Equations 7 and 8 have to be verified at each time step; thus, it is convenient to consider differentiation with respect to time of such equations:

$$\dot{s}_{xx} = \frac{E}{1-\upsilon^2}\;\left[\dot{\varepsilon}_{xx} + \nu\dot{\varepsilon}_{yy}\right] - \frac{E}{1-\nu}\dot{\epsilon}^j \tag{12}$$

$$\dot{s}_{yy} = \frac{E}{1-\upsilon^2}\;\left[\dot{\varepsilon}_{yy} + \nu\dot{\varepsilon}_{xx}\right] - \frac{E}{1-\nu}\,\dot{\epsilon}^j \tag{13}$$

where (E) and ν were assumed to be constant.

Before the shrinkage starts, the stress depends on ε^j in particular:

$$s_{ii} = \int_{t_s}^{t} -\frac{E}{1-\nu}\dot{\epsilon}^j dt \tag{14}$$

where t_s is the time at which solidification starts. As soon as the shrinkage starts, the average stress has to satisfy the force balance (given along the x direction).

$$\int_0^D \sigma_{xx} dz = \int_0^{z_s} s_{xx}^{solid} dz \; - (D - z_s) P\;(t) = F_{w.x}\;(t) + F_{fr.x}\,(t) \tag{15}$$

The term $(D - z_s)P(t)$ represents the stretching force exerted by the melt on the solid. The force balance is obtained if the force due to the stress is equal to the summation of the force exerted by the cavity confining the polymer (the model was developed for injection molding), F_w, and the friction force, F_{fr}, (see also Figure 17):

The forces involved in the balance change as the process (the solidification) proceeds; thus the force evolution has to be accounted for. To this purpose, the first derivative of the force due to the stress can be introduced (Equation 16).

$$\frac{d}{dt} \int_0^{z_s} s_{xx}^{solid} dz = \int_0^{z_s} \dot{s}_{xx}^{solid} dz + s_{xx}^{solid}\,(z_s,\; t)\,\dot{z}_s \tag{16}$$

$\dot{z}_s$ is the formation rate of the solid layer, $s_{xx}^{solid}(z_s,\; t)$ belonged to the stress without the pressure contributions at the solid-melt interface and it is equal to the zero, $\dot{s}_{xx}^{solid}$ is the stress rate. To obtain the stress evolution it is required to know temperature and pressure evolutions, pressure–volume–temperature behavior of the polymer, mechanical constants, and a solidification criterion to identify t_s.

In the next steps, shrinkage was calculated in both solid and molten part.

$$\delta_x\,(t)_0^t = \left(\frac{1}{L} \int_0^L \varepsilon_{xx}^s dx \right)_0^t \quad \text{solidified layer} \tag{17}$$

$$\delta_y\,(t)_0^t = \left(\frac{1}{W} \int_0^W \varepsilon_{yy}^s dy \right)_0^t \quad \text{solidified layer} \tag{18}$$

$$\delta_z\,(t)_0^t = \frac{1}{D} \left(\int_0^{z_s} \varepsilon_{zz}^s dz + \int_{z_s}^D \varepsilon_{zz}^f dz \right)_0^t \quad \text{solid and fluid} \tag{19}$$

δ_x and δ_y represent the shrinkage along with the length and width directions, while the δ_z is the total thickness shrinkage. The model mentioned above was applied to injection molding to assess deformation due to shrinkage, with the right assumptions, it can be used for describing the same phenomenon in MEAM.

Table 4 summarizes the model reported in the literature for the description of the main phenomena leading warpage. In the table, the first column is related to the energy balance, which is used to describe the cooling during deposition; in some cases, radiation has been accounted for. The following columns are related to the approaches adopted for the description of part deformation:

- Force: referred to the force balance to account for the stress distribution arising during cooling. These models account for the effect of volume contraction due to solidification.
- Stress relaxation: consider the relaxation of stresses accumulated in the material due to the presence of a convergent geometry at the nozzle exit;
- Crystallization: models accounting for incoming crystallization during deposition are introduced;
- Effect of the flow rate: model that accounts for the effect of the flow rate inside the liquefier on the part thickness.
- Adhesion between the part and bed: model accounting for surface interaction between bed and part.

Table 4 also reports the validation strategy adopted for each model. In most cases, the validation is not accurate or limited to simple geometries and a small number of deposited layers.

Wang et al. [188] calculated the stress from the force and momentum balance in the MEAM process. They neglected the pressure contribution and did not consider crystallization since it is negligible for the considered polymer in the operating temperature range. The temperature field and printing speed influence the stress in each deposited bead. They consider that there is no stress at the nozzle exit and that deformation occurs between the glass transition temperature and the chamber temperature. Each layer can deform independently of the deposition of the other layers. However, each new layer is deposited on a previously deposited layer, undergoing contraction. The net force of the body and the momentum must be equal to zero [186]. To achieve such a condition, the bending stress, E(z−d)/R, where d is the position of the neutral axis and R is the radius of curvature has to be considered. To satisfy the condition of zero summation of forces, a constant stress σ^* is introduced. The final stress state in the part is given by Equation 20:

$$\sigma = -E\alpha\Delta T + \sigma^* + \frac{E\,(z - d)}{R} \tag{20}$$

$$\varepsilon = \frac{\sigma^*}{E} + \frac{(z - d)}{R} \tag{21}$$

Wang's model considers only thermal stress. In Equation 20, ε is the thermal strain, σ thermal stress, α is the linear shrinkage coefficient coming from the pressure–volume–temperature behavior of the material, E represents the elastic modulus of the material. The average force and momentum are expressed as integrals across the layer thickness h:

$$\int_0^h \left(-E\alpha\Delta T + \sigma^* + \frac{E\,(z - d)}{R} \right) dz = 0 \tag{22}$$

$$\int_0^h \left(-E\alpha\Delta T + \sigma^* + \frac{E\,(z - d)}{R} \right) z dz = 0 \tag{23}$$

TABLE 4 | Models reported in the literature for the description of the main phenomena leading to warpage.

Model	Energy	Radiation	Force	Stress relaxation	Crystallization	Effect of the flow rate inside the extruder	Adhesion between the plate and the part	Material	validation
Wang et al. [188]	✓	×	✓	×	×	✓	×	ABS	Only in case of thin wall prototype
Armillotta et al. [21]	✓	×	✓	×	×	✓	✓	ABS	Poor accuracy in case of long parts
Wijnen et al. [189]	✓	×	✓	×	×	×	×	PLA	Not accurate for the first layers
Ergene et al. [190]	✓	×	✓	×	×	×	×	ABS	93% of accuracy in all conditions
Jiang et al. [191]	✓	✓	✓	✓	✓	×	×	SCF/PLA	none
Watanabe et al. [192]	✓	×	✓	✓	✓	×	×	PP	Only for the short length and low number of layers
Fitzharris et al. [37]	✓	×	✓	✓	✓	×	×	PPS	Only for the short length and low number of layers
Xinhua et al. [86]	✓	×	✓	×	×	✓	×	PLA	Not for the large dimension and thin part
Yu et al. [27]	✓	✓	✓	✓	✓	✓	×	PP	Good accuracy for thick wall
Samy et al. [193]	✓	×	✓	✓	✓	✓	✓	PP	Accurate for all condition
Chen et al. [194]	✓	×	✓	×	×	×	×	ABS	Accurate for the square and circle sheets
Zhang et al. [195]	✓	×	✓	×	✓	×	×	ABS	none
Cattenone et al. [196]	✓	✓	✓	✓	×	×	×	ABS	Deformation is predicted
Banerjee et al. [197]	✓	×	✓	×	×	×	×	—	none
Syrlybayev et al. [198]	✓	✓	✓	×	×	✓	×	ABS	Accurate for thick parts

They calculated the warp deformation from the radius of curvature as given in Equation 24:

$$\delta = R\left(1 - cos\frac{L}{2R}\right) = \frac{n^3\Delta h}{6\alpha\left(T_g - T_e\right)(n-1)} \times \left\{1 - \cos\left[\frac{3\alpha L}{n\Delta h}\left(T_g - T_e\right)\frac{n(n-1)}{n^2}\right]\right\} \quad (24)$$

where L is the section length of the layers, δ is the warp deformation, n is the number of the deposited layers and Δh is the thickness of each deposited layer. T_g and T_e are the glass transition and chamber temperature, respectively. The researchers proposed a case study to validate their model using a car lamp prototype: the observed average deformation along the selected direction (0.32 mm) closely matched the predicted range (0.2–0.4 mm).

Armillotta et al. [21] studied warpage in MEAM of ABS thermoplastic by using Wang et al. [188] model and focused on the effects of part dimensions and layer height. They also consider the plastic contribution to deformation, which means that the material overcomes the yield stress and assumes a plastic behavior. They analyzed thermal stress propagation across layers and bending stresses exceeding the material's yield point. The experimental data also confirmed the nonlinear relationships between the part dimension and warpage. Although the approach could predict the deformation trends in the presence of multiple layers and different thicknesses, some discrepancies between the experimental data and simulations are still present, especially in the case of long parts.

Wijnen et al. [189] used Wang's approach to predict warpage during PLA part printing [188]. The modified model accounted for conduction and convection in the heat transfer. They validated their model through comparison between the recorded temperature during printing and the predicted one, then applied the model for the description of the stress evolution. Their results demonstrated that the model is reliable in predicting the deformation of high vertical walls (namely high number of layers) of PLA. However, it shows a limited accuracy in the case of few layers. Moreover, they investigated the effect of annealing and found that the deposition plate temperature should be kept at 50°C or lower to avoid shrinkage due to crystallization.

Ergene et al. [190] used Digimat AM 2021 software, a purpose-built program for additive manufacturing simulation accounting for Wang's model [188], to analyze the effects of fiber amount, infill density, and infill pattern on warpage of ABS parts made via MEAM. They found that a higher fiber amount and infill density reduced warpage but increased residual stresses due to increased rigidity and polymer–fiber interaction.

A similar approach was followed by Jiang et al. [191], who analyzed the effect of part shape on the deformation ongoing during MEAM. They examined the residual stress, crystallinity, and warpage in square (ST) and circular (CT) parts made in PLA. Their results showed higher stress and warpage in ST than in CT due to edge effects, with crystallinity decreasing from the bottom to the top layers.

Watanabe et al. [192] proposed a model that accounts for the temperature evolution inside the deposited filaments, taking the viscosity as a shear rate and temperature function. Their model, developed in ANSYS Polyflow, accounted for the temperature evolution during the cooling of the first two deposited layers and takes into account the conduction heat transfer between these two layers. The predicted temperature evolution was used in the model to evaluate stress evolution, which model is built in ANSYS Mechanical, to determine the residual stress and warpage caused by the crystallization of the material during the cooling process. They applied the model to the PP printing. Specific alterations in processing parameters can significantly impact dimensional accuracy. Their simulations were found to be essentially consistent with the experimental data.

Fitzharris et al. [37] described the evolution of stress in polyphenylene sulfide (PPS) parts. PPS is a high-performance semicrystalline polymer with high-temperature resistance. They assumed that the higher processing temperature increases the warpage due to the faster cooling. Their simulation suggested that the thermal expansion coefficient, heat capacity, and the elastic modulus determine the warpage values: by reducing the thermal expansion coefficient (for instance, through the introduction of suitable fillers), the warpage decreases. The model was validated in the case of a small number of deposited layers.

Xinhua et al. [86] applied a model for stress evolution description to a thin plate of PLA. They included thermoelastic behavior in the model and were able to forecast deformations in the selected part. They assumed that each layer is deposited instantaneously, resulting in a uniform temperature within the layer. They also assumed that the printing and shrinking of filament feedstock occur simultaneously within a single layer. The final deflection model for predicting the warpage in 2D is given in Equation 25:

$$w\ (x,\ y) = \frac{6\alpha\left(T_g - T_e\right)(2n-1)(1+\nu)}{\delta_0 n^3}\left(x^2 + y^2\right) \quad (25)$$

where T_g and T_e are glass and chamber temperature, respectively, n is the number of layers, h is the layer thickness, and ν is the Poisson's ratio. To validate their model, they compare experimental deformation, measured through a 3D laser scanner, with calculated deformation. The findings substantiated the accuracy of the theoretical model and yielded optimal processing conditions for minimizing warpage.

Yu et al. [27] focused on developing a computational model based on the Jiang et al. [191] findings in MEAM to predict the behavior of rectangular PP boxes with different thicknesses. The researchers account for the heat transfer due to radiation and conduction, and the thermoelastic behavior of the material to predict the stress evolution. Furthermore, crystallization during the process was also considered. Their results show that thicker parts have higher average crystallinity. Both experimental and simulated data demonstrated that thicker parts are characterized by less warpage (1.6 mm) compared to thinner specimens (5.9 mm).

Sreejith et al. [40] developed a model based on the thermodynamic principles, including free energy and entropy production.

This approach boosts the prediction of stress and geometry changes during the process.

Samy et al. [193] analyzed the effect of different printing parameters (chamber temperature, layer number, and printing speed) on PP 3D printed parts. A 3D model was built in COMSOL Multiphysics and accounts for the heat transfer during deposition and the non-isothermal crystallization kinetics. The model was validated by comparing the predicted temperature evolution with the temperature evolution recorded at the first layer. Their simulations indicated that the semicrystalline nature and thermo–mechanical history significantly affect the residual stress in 3D printed parts. The warpage predicted from the simulations was compared with that found in the final parts (evaluated using a 3D scanner); and it was consistent with the experimental one.

Chen et al. [194] developed a simulation framework using thermal-structural analysis with a finite element method coupled in ANSYS to predict warping in MEAM for ABS. Their model considers only conduction and convection in the heat transfer. Their analysis was conducted in two steps: initially, a thermal evaluation was simulated; then, the outcomes from heat transfer were utilized as input to perform a structural analysis, which yielded the stress and strain distribution over the part. Their findings highlight the significant impact of thermal gradient-induced stresses on part distortion, particularly for angular shapes and diagonal infill line directions. Their model was validated in the case of simple geometries.

Zhang et al. [195] employed a FEA model [199] to simulate the ABS deposition by using ANSYS. This model couples thermal and mechanical aspects, utilizing an element activation function to simulate deposition of new layers. The results coming from the simulation suggested that the tool path influences the deflection of the part. In particular, the 90° raster angle gave a smaller residual stress than 0° raster angle. Experimental distortions of 3D printed parts were found to be comparable to the predicted distortion, although a quantitative correlation was not established.

Cattenone et al. [196] used ABAQUS software to perform a simulation in the meso/macroscopic scale of the MEAM process for ABS. They adopted the additive decomposition of the strain already mentioned. Their model also considered heat flow due to convection and radiation. Because of the temperature gradients, the filaments exchange thermal energy with both the previously deposited material and the surrounding environment. The predicted temperature evolutions and deformation were found to be consistent with the experimental ones.

Banerjee et al. [197] investigated the effect of the MEAM process parameters, such as deposited filament width (it depends on the flow rate once the layer height and extrusion ratio are fixed), part orientation (with respect to construction direction), part length, and part width, on the warpage amount. They built a thermal and structural model in MATLAB R2017a to determine the impact of the printing parameters on the geometrical accuracy of the 3D printed parts and select proper design and process parameters prior to printing.

Syrlybayev et al. [198] developed a thermomechanical model built in ANSYS Mechanical to simulate the deposition in the MEAM process and predict warpage. Warpage was mainly attributed to the nonuniform internal stresses caused by rapid heating and cooling during printing. The model was validated through comparison with experimental data, in particular, the warped edge. The model accurately predicted the warpage dependence on layer height, deposition plate, and nozzle temperatures.

8 | Conclusions and Future Outlooks

8.1 | Conclusions

Material Extrusion Additive Manufacturing (MEAM) provides significant flexibility regarding material selection, encompassing both amorphous and semicrystalline polymers, and finds extensive application across multiple industrial sectors. One significant challenge associated with MEAM is warpage, which refers to a geometric deformation that takes place during the cooling process, thereby impacting the precision and quality of the printed components.

Understanding of the intricate thermomechanical processes that take place during the printing procedure is essential for minimizing warpage. The observed deformations primarily result from internal stresses induced by thermal gradients and variations in specific volume during the cooling process. Thermoplastic polymers exhibit warpage influenced by their inherent material properties. Amorphous polymers, with a disordered molecular structure, typically demonstrate reduced warpage compared to semicrystalline polymers, which experience additional contraction during cooling due to crystallization.

Various measurement techniques have been developed to quantify and analyze warpage, including both ex-situ and in-situ methods. Ex-situ methods, including standardized geometries like rectangular plates, cylindrical disks, and cantilever beams, facilitate the evaluation of the final deformations of printed components. Conversely, in-situ techniques like digital image correlation, strain gauges, and optical interferometry methods provide real-time monitoring of warpage during the printing process, facilitating immediate adjustments to enhance part quality.

In the case of amorphous polymers like ABS and PLA, warpage is primarily affected by factors including nozzle temperature, deposition plate temperature, and printing speed. A deposition plate temperature near the polymer's glass transition temperature decreases thermal gradients and internal stress, thereby reducing warpage. Crystallization kinetics are critical in the warpage of semicrystalline polymers, including polypropylene (PP) and polyamide (PA). Rapid crystallization may result in elevated internal stresses; however, careful regulation of temperatures and cooling rates can alleviate these issues.

Modelling warpage makes it possible to predict and reduce the deformation caused by the multitude of parameters involved. It avoids the high costs associated with testing by simulating thermal and mechanical stress. It allows the prediction of defor-

mation and residual stress using numerical simulations, as well as thermomechanical models that provide a detailed description of stress evolution. Models validated by experiments can be used to optimize printing parameters, ensuring greater precision and quality in the manufactured parts.

In summary, a thorough comprehension of warpage in MEAM is essential for enhancing the quality and accuracy of 3D printed components. Ex-situ and in-situ measurement techniques facilitate the analysis and prediction of deformation, providing tools to optimize printing parameters based on the properties of amorphous and semicrystalline polymers, for a significant reduction in the warpage. By summarizing current knowledge and highlighting important research gaps, the aim of this review is to propose a conceptual framework for improving the understanding and control of the warpage phenomenon in MEAM, which could encourage its wider adoption in high-precision manufacturing industries.

8.2 | Future Outlooks

Future research on warpage in MEAM should focus on developing advanced and targeted strategies for prediction, monitoring, and controlling this issue. One promising direction is the use of machine learning-based prediction models, which can forecast deformation patterns by analyzing large datasets of printing parameters and warpage outcomes. Critical research gaps remain, particularly in the area of multi-scale modeling, where it is necessary to link molecular-level mechanisms (such as polymer crystallization) to macro-scale deformation. Further innovation in material development, in particular the creation of polymers with tailored crystallization kinetics or enhanced thermal shrinkage, could also play a key role in minimizing warpage. Additionally, hybrid modeling approaches that combine finite element simulations with data-driven techniques and the integration of process modeling with CAD tools will be essential for enabling predictive design and true manufacturing optimization. Addressing these challenges will support the wider adoption of MEAM in precision-demanding industries.

Acknowledgements

This work received financial support from the European Union–Next Generation EU–PNRR M4/C2/INVESTIMENTO.1.1, in the frame of the PRIN 2022 programme (D.D. 104, 02-02-2022), Project 2022MMTBMJ "Zero-defect Fused Filament Fabrication" (0DeF^3), ERC field PE11, CUP D53D23005420006.

Open access publishing facilitated by Universita degli Studi di Genova, as part of the Wiley - CRUI-CARE agreement.

Conflicts of Interest

The authors declare no conflict of interest.

Endnotes

[1] Infill denotes the internal structure present within the printed parts, with the effect of infill density on warpage detailed in Section 5.

References

1. A. Costanzo, D. Cavallo, and C. McIlroy, "High-Performance Co-Polyesters for Material-Extrusion 3D Printing: A Molecular Perspective Of Weld Properties," *Additive Manufacturing* 49 (2022): 102474.

2. A. Costanzo, R. Spotorno, M. V. Candal, et al., "Residual Alignment and its Effect on Weld Strength in Material-Extrusion 3D-Printing of Polylactic Acid," *Additive Manufacturing* 36 (2020): 101562.

3. M. Jin, C. Neuber, and H. W. Schmidt, "Tailoring Polypropylene for Extrusion-Based Additive Manufacturing," *Additive Manufacturing* 33 (2020): 101101.

4. D. A. J. Brion, M. Shen, and S. W. Pattinson, "Automated Recognition and Correction of Warp Deformation in Extrusion Additive Manufacturing," *Additive Manufacturing* 56 (2022): 102838.

5. T. Schuller, M. Jalaal, P. Fanzio, and F. J. Galindo-Rosales, "Optimal Shape Design of Printing Nozzles for Extrusion-Based Additive Manufacturing," *Additive Manufacturing* 84 (2024): 104130.

6. Market Research Intellect, Fused Filament Fabrication(FFF) 3D Printer Market Size By Product By Application By Geography Competitive Landscape And Forecast, accessed: July 1, 2025, https://www.marketresearchintellect.com/product/fused-filament-fabrication-fff-3d-printer-market/#:%7E;:text=The%20Fused%20Filament%20Fabrication%20%28FFF%29%203D%20Printer%20Market,a%20CAGR%20of%2020.5%25%20from%202025%20to%202032.

7. J. I. Aguilar-Duque, J. L. Garcia, and J. L. Hernández-Arellano, Additive Manufacturing Using Fused Filament Fabrication: Evolution and Trends, (2021), https://doi.org/10.21203/rs.3.rs-234581/v1.

8. F. Kappmeier, *Market Usage Gap Analysis– Market Potential, Target Group Classification and Penetration Strategy for Large Scale Fused Filament Fabrication Machines in Germany* (Hamburg University of Applied Sciences, 2018).

9. H. He, Z. Zhu, Y. Zhang, Z. Zhang, T. Famakinwa, and R. Yang, "Machine Condition Monitoring For Defect Detection in Fused Deposition Modelling Process: A Review," *The International Journal of Advanced Manufacturing Technology* 132 (2024): 3149–3178.

10. A. Breckwoldt Jurado and D. Golzio, "The Interplay Between Universities and Companies. A Case Study in the Field of 3D Printing," *World Patent Information* 77 (2024): 102267.

11. M. Spoerk, J. Gonzalez-Gutierrez, C. Lichal, et al., "Optimisation of the Adhesion of Polypropylene-Based Materials During Extrusion-Based Additive Manufacturing," *Polymers* 10 (2018): 490.

12. W. Ju, X. Gao, Y. Su, F. Luo, and D. Wang, "Direct Relationship Between Crystalline Structure and Part Deformation of Polypropylene Copolymer Parts Fabricated by Material Extrusion Additive Manufacturing," *Journal of Polymer Science* 61 (2023): 2665–2676.

13. Y.-H. Choi, C.-M. Kim, H.-S. Jeong, and J.-H.o Youn, "Influence of Bed Temperature on Heat Shrinkage Shape Error in FDM Additive Manufacturing of the ABS-Engineering Plastic," *World Journal of Engineering and Technology* 04 (2016): 186–192.

14. M. S. Andrés, R. Chércoles, E. Navarro, et al., "Use of 3D Printing PLA and ABS Materials for Fine Art. Analysis of Composition and Long-Term Behaviour of Raw Filament and Printed Parts," *Journal of Cultural Heritage* 59 (2023): 181–189.

15. X. Gao, S. Qi, X. Kuang, Y. Su, J. Li, and D. Wang, "Fused Filament Fabrication of Polymer Materials: A Review of Interlayer Bond," *Additive Manufacturing* 37 (2021): 101658.

16. A. Jandyal, I. Chaturvedi, I. Wazir, A. Raina, and M. I. Ul Haq, "3D printing—A Review of Processes, Materials and Applications in Industry 4.0," *Sustainable Operations and Computers* 3 (2022): 33–42.

17. A. Bayati, M. Ahmadi, D. Rahmatabadi, et al., "3D Printed Elastomers with Superior Stretchability and Mechanical Integrity by Parametric Optimization of Extrusion Process Using Taguchi Method," *Materials Research Express* 12 (2025): 015301.

18. A. Das, J. S. Bryant, C. B. Williams, and M. J. Bortner, "Melt-Based Additive Manufacturing of Polyolefins Using Material Extrusion and Powder Bed Fusion," *Polymer Reviews* 63 (2023): 895–960.

19. M. Spoerk, C. Holzer, and J. Gonzalez-Gutierrez, "Material Extrusion-Based Additive Manufacturing of Polypropylene: A Review on How to Improve Dimensional Inaccuracy and Warpage," *Journal of Applied Polymer Science* 137 (2020): 48545.

20. P. Honari, D. Rahmatabadi, A. Bayati, et al., "Simultaneous 4D Printing and In-Situ Foaming for Tailoring Shape Memory Behaviors in Polylactic Acid Foams," *Manufacturing Letters* 43 (2025): 33–36.

21. S. Qi, X. Gao, Y. Su, X. Dong, D. Cavallo, and D. Wang, "Correlation Between Welding Behavior and Mechanical Anisotropy of Long Chain Polyamide 12 Manufactured with Fused Filament Fabrication," *Polymer* 213 (2021): 123318.

22. N. Verma, P. Awasthi, A. Gupta, and S. S. Banerjee, "Fused Deposition Modeling of Polyolefins: Challenges and Opportunities," *Macromolecular Materials and Engineering* 308 (2023): 2200421.

23. F. Christakopoulos, P. M. H. van Heugten, and T. A. Tervoort, "Additive Manufacturing of Polyolefins," *Polymers* 14 (2022): 5147.

24. A. A. Rosli, R. K. Shuib, K. M. K. Ishak, Z. A. A. Hamid, M. K. Abdullah, and A. Rusli, "Influence of Bed Temperature on Warpage, Shrinkage and Density of Various Acrylonitrile Butadiene Styrene (ABS) Parts From Fused Deposition Modelling (FDM)," *AIP Conference Proceedings* 2267 (2020): 020072.

25. A. Armillotta, M. Bellotti, and M. Cavallaro, "Warpage of FDM parts: Experimental tests and analytic model," *Robotics and Computer-Integrated Manufacturing* 50 (2018): 140–152.

26. V. V. Bhandarkar, A. Kumar, and P. Tandon, "Warpage Detection in 3D Printing of Polymer Parts: A Deep Learning Approach," *Journal of Intelligent Manufacturing* 36 (2024): 3129.

27. Y. Yu, B. Jiang, Y. Chen, and L. Ye, "Modelling and Characterising FFF Process of Semi-Crystalline Polymers: Warpage Formation and Mechanism Analysis," *Polymers and Polymer Composites* 32 (2024).

28. M. Jin, R. Giesa, C. Neuber, and H. W. Schmidt, "Filament Materials Screening for FDM 3D Printing by Means of Injection-Molded Short Rods," *Macromolecular Materials and Engineering* 303 (2018): 1800507.

29. C. McIlroy and R. S. Graham, "Modelling Flow-Enhanced Crystallisation During Fused Filament Fabrication of Semi-Crystalline Polymer Melts," *Additive Manufacturing* 24 (2018): 323–340.

30. L. A. Northcutt, S. V. Orski, K. B. Migler, and A. P. Kotula, "Effect of Processing Conditions on Crystallization Kinetics During Materials Extrusion Additive Manufacturing," *Polymer* 154 (2018): 182–187.

31. C. O. Ufodike and G. C. Nzebuka, "Investigation of Thermal Evolution and Fluid Flow in the Hot-End of a Material Extrusion 3D Printer Using Melting Model," *Additive Manufacturing* 49 (2022): 102502.

32. F. Peng, B. D. Vogt, and M. Cakmak, "Complex Flow and Temperature History During Melt Extrusion in Material Extrusion Additive Manufacturing," *Additive Manufacturing* 22 (2018): 197–206.

33. D. Vaes and P. Van Puyvelde, "Semi-crystalline feedstock for filament-based 3D printing of polymers," *Progress in Polymer Science* 118 (2021): 101411.

34. M. Pourali and A. M. Peterson, "Thermal Modeling of Material Extrusion Additive Manufacturing, in: Polymer-Based Additive Manufacturing: Recent Developments," *American Chemical Society* 1315 (2019): 115–130.

35. P. P. Parlevliet, H. E. N. Bersee, and A. Beukers, "Residual Stresses in Thermoplastic Composites—A Study of the Literature—Part I: Formation of Residual Stresses," *Composites Part A: Applied Science and Manufacturing* 37 (2006): 1847–1857.

36. C. Kousiatza and D. Karalekas, "In-Situ Monitoring of Strain and Temperature Distributions During Fused Deposition Modeling Process," *Materials and Design* 97 (2016): 400–406.

37. E. R. Fitzharris, N. Watanabe, D. W. Rosen, and M. L. Shofner, "Effects of Material Properties on Warpage in Fused Deposition Modeling Parts," *The International Journal of Advanced Manufacturing Technology* 95 (2018): 2059–2070.

38. B. N. Turner and S. A. Gold, "A Review of Melt Extrusion Additive Manufacturing Processes: II. Materials, Dimensional Accuracy, and Surface Roughness," *Rapid Prototyping Journal* 21 (2015): 250–261.

39. M. Spoerk, J. Sapkota, G. Weingrill, T. Fischinger, F. Arbeiter, and C. Holzer, "Shrinkage and Warpage Optimization of Expanded-Perlite-Filled Polypropylene Composites in Extrusion-Based Additive Manufacturing," *Macromolecular Materials and Engineering* 302 (2017): 1700143.

40. P. Sreejith, K. Kannan, and K. Rajagopal, "A Thermodynamic Framework for Additive Manufacturing, Using Amorphous Polymers, Capable of Predicting Residual Stress, Warpage and Shrinkage," *International Journal of Engineering Science* 159 (2021): 103412.

41. A. Shrivastava, "Introduction to Plastics Engineering," in *Introduction to Plastics Engineering*, ed. A. Shrivastava (William Andrew Publishing, 2018), 1–16.

42. A. Deghiche, N. Haddaoui, A. Zerriouh, et al., "Effect of the stearic acid-modified TiO2 on PLA nanocomposites: Morphological and thermal properties at the microscopic scale," *Journal of Environmental Chemical Engineering* 9 (2021): 106541.

43. N. S. Zaki and T. W. Salih, "The Effect of Crystallinity on the Thermal Conductivity of Polymer," *Journal of Engineering and Sustainable Development* 25 (2021): 2–25.

44. A. Belhaoues, W. Benayache, A. Zerriouh, and S. Benmesli, "Experimental and Theoretical Investigation of the Effect of Physical and Chemical Compatibilization on the Properties of Thermoplastic Elastomers Derived From Natural Rubber and Polypropylene Blends," *Materials Today Communications* 40 (2024): 109420.

45. A. Belhaoues, A. Zerriouh, W. Benayache, and A. Benaissa, "Excellent Compatibilization Effect of (ENR/PP-g-MA) as a Dual Reactive Compatibilizer on the Immiscible Thermoplastic Elastomer Based on Nitrile Rubber and Polypropylene Blends: Insights From Experimental and Computational Studies," *Materials Today Communications* 42 (2025): 111336.

46. W. Benayache, M. T. Benaniba, and Z. Ali, "Theoretical and Experimental Investigation of the Compatibilization Agent Contribution to the Interactions of Polymer Blend (PP /LDPE): Thermal, Morphological, and DFT Insights," *Journal of Molecular Liquids* 394 (2024): 123745.

47. N. Bachhar, A. Gudadhe, A. Kumar, P. Andrade, and G. Kumaraswamy, "3D printing of Semicrystalline Polypropylene: Towards Eliminating Warpage of Printed Objects," *Bulletin of Materials Science* 43 (2020): 171.

48. J. Sun, X. Liao, A. M. Minor, N. P. Balsara, and R. N. Zuckermann, "Morphology-Conductivity Relationship in Crystalline and Amorphous Sequence-Defined Peptoid Block Copolymer Electrolytes," *Journal of American Chemical Society* 136 (2014): 14990–14997.

49. W. Yan, L. Fang, M. Heuchel, K. Kratz, and A. Lendlein, "Modeling of Stress Relaxation of a Semi-Crystalline Multiblock Copolymer and its Deformation Behavior," *Clinical Hemorheology and Microcirculation* 60 (2015): 109–120.

50. T. Ageyeva, I. Sibikin, and J. G. Kovács, "Review of Thermoplastic Resin Transfer Molding: Process Modeling and Simulation," *Polymers* 11 (2019): 1555.

51. V. R. Sastri, "Materials Used in Medical Devices," in *Plastics in Medical Devices*, ed. V.R. Sastri, 2nd ed. (William Andrew Publishing, 2014): 19–31.

52. C. Yan, Y. Shi, and L. Hao, "Investigation into the Differences in the Selective Laser Sintering between Amorphous and Semi-crystalline Polymers," *International Polymer Processing* 26 (2011): 416–423.

53. M. Moretti and N. Senin, "In-Process Monitoring of Part Warpage in Fused Filament Fabrication Through the Analysis of the Repulsive Force Acting on the Extruder," *Additive Manufacturing* 49 (2022): 102505.

54. H. Janeschitz-Kriegl, Polymer Crystallization under Process Conditions, in *Rheological Fundamentals of Polymer Processing*, eds. J. A. Covas, J. F. Agassant, A. C. Diogo, J. Vlachopoulos, K. Walters (Springer Netherlands, 1995), 423–436.

55. H. Zuidema, G. W. M. Peters, and H. E. H. Meijer, "Influence of Cooling Rate on pVT-Data of Semicrystalline Polymers," *Journal of Applied Polymer Science* 82 (2001): 1170–1186.

56. F. He, M. Khan, and S. Aldosari, "Interdependencies between Dynamic Response and Crack Growth in a 3D-Printed Acrylonitrile Butadiene Styrene (ABS) Cantilever Beam under Thermo-Mechanical Loads," *Polymers* 14 (2022): 982.

57. Z. Yang, F. He, and M. Khan, "An Empirical Torsional Spring Model for the Inclined Crack in a 3D-Printed Acrylonitrile Butadiene Styrene (ABS) Cantilever Beam," *Polymers* 15 (2023): 496.

58. C. Chung Wang, T.a-W. Lin, and S.-S. Hu, "Optimizing the Rapid Prototyping Process by Integrating the Taguchi Method with the Gray Relational Analysis," *Rapid Prototyping Journal* 13 (2007): 304–315.

59. A. Noriega, D. Blanco, B. J. Alvarez, and A. Garcia, "Dimensional Accuracy Improvement of FDM Square Cross-Section Parts Using Artificial Neural Networks and an Optimization Algorithm," *International Journal of Advanced Manufacturing Technology* 69 (2013): 2301–2313.

60. C. Ziemian and P. Crawn III, Computer Aided Decision Support For Fused Deposition Modeling, http://www.emerald-library.com/ft.

61. D. Croccolo, M. De Agostinis, S. Fini, M. Mele, G. Olmi, and G. Campana, "Effects of Infill Temperature on the Tensile Properties and Warping of 3D-Printed Polylactic Acid," *Progress in Additive Manufacturing* 9 (2023): 919–934.

62. R. Singh, "Some Investigations for Small-Sized Product Fabrication with FDM for Plastic Components," *Rapid Prototyping Journal* 19 (2013): 58–63.

63. E. H. Tümer and H. Y. Erbil, "Extrusion-Based 3D Printing Applications of pla Composites: A Review," *Coatings* 11 (2021): 390.

64. F. He, Y. L. A. Alshammari, and M. Khan, "The Effect of Printing Parameters on Crack Growth Rate of FDM ABS Cantilever Beam under Thermo-mechanical Loads," *Procedia Structural Integrity* (Elsevier B.V., 2021): 59–64.

65. M. Aizzat, Z. Anwar, P. P. A. Majeed, M. Hasnun, and A. Hassan, Lecture Notes in Mechanical Engineering, n.d. http://www.springer.com/series/11693.

66. P. Geng, J. Zhao, W. Wu, et al., "Effects of Extrusion Speed and Printing Speed on the 3D Printing Stability of Extruded PEEK filament," *Journal of Manufacturing Processes* 37 (2019): 266–273.

67. M. Arhant, N. Meek, D. Penumadu, P. Davies, and N. Garg, "Residual Strains using Integrated Continuous Fiber Optic Sensing in Thermoplastic Composites and Structural Health Monitoring," *Experimental Mechanics* 58 (2018): 167–176.

68. A. Kantaros and D. Karalekas, "Fiber Bragg Grating Based Investigation of Residual Strains in ABS Parts Fabricated by Fused Deposition Modeling Process," *Materials and Design* 50 (2013): 44–50.

69. A. M. L. Lanzolla, F. Attivissimo, G. Percoco, M. A. Ragolia, G. Stano, and A. Di Nisio, "Additive Manufacturing for Sensors: Piezoresistive Strain Gauge with Temperature Compensation," *Applied Sciences* 12 (2022): 8607.

70. G. Stano, A. Di Nisio, A. Lanzolla, and G. Percoco, "Additive Manufacturing and Characterization of a Load Cell with Embedded Strain Gauges," *Precision Engineering* 62 (2020): 113–120.

71. V. Matveenko, N. Kosheleva, and G. Serovaev, "Measurement of Strain and Temperature by Fiber-Optic Sensors Embedded into Samples Manufactured by Additive Technology," *Procedia Structural Integrity* (Elsevier B.V., 2022): 307–314.

72. M. Jani, S. Chava, J. Brown, and S. Namilae, "In-Situ Monitoring of Additive Manufacturing using Digital Image Correlation," in *AIAA Science and Technology Forum and Exposition, AIAA SciTech Forum 2022*, (American Institute of Aeronautics and Astronautics Inc, AIAA, 2022).

73. R. D. Murphy and E. C. Forrest, A Review of In-situ Temperature Measurements for Additive Manufacturing Technologies, 2016.

74. R. Spencer, A. A. Hassen, J. Baba, et al., "An Innovative Digital Image Correlation Technique for In-Situ Process Monitoring of Composite Structures in Large Scale Additive Manufacturing," *Composite Structures* 276 (2021): 114545.

75. K. Khanafer, J. Cao, and H. Kokash, "Condition Monitoring in Additive Manufacturing: A Critical Review of Different Approaches," *Journal of Manufacturing and Materials Processing* 8 (2024): 95.

76. S. Wang, K. Lasn, C. W. Elverum, D. Wan, and A. Echtermeyer, "Novel In-Situ Residual Strain Measurements in Additive Manufacturing Specimens by Using the Optical Backscatter Reflectometry," *Additive Manufacturing* 32 (2020): 101040.

77. J. X. J. Zhang and K. Hoshino, "Mechanical Transducers: Cantilevers, Acoustic Wave Sensors, and Thermal Sensors," in *Molecular Sensors and Nanodevices*, eds. J.X.J. Zhang, K. Hoshino, 2nd ed. (Academic Press, 2019): 311–412.

78. V. Matveenko, N. Kosheleva, and G. Serovaev, "Measurement of Strain and Temperature by Fiber-Optic Sensors Embedded into Samples Manufactured by Additive Technology," *Procedia Structural Integrity* 42 (2022): 307–314.

79. M. Mukhtarkhanov, E. Shehab, and M. H. Ali, "Experimental Study on Warpage Phenomenon of Wax Parts Manufactured by Fused Filament Fabrication," *Polymers* 16 (2024): 208.

80. Z. Jin, Z. Zhang, and G. X. Gu, "Automated Real-Time Detection and Prediction of Interlayer Imperfections in Additive Manufacturing Processes Using Artificial Intelligence," *Advanced Intelligent Systems* 2 (2020): 1900130.

81. S. Wang, K. Lasn, C. W. Elverum, D. Wan, and A. Echtermeyer, "Novel In-Situ Residual Strain Measurements in Additive Manufacturing Specimens by Using the Optical Backscatter Reflectometry," *Additive Manufacturing* 32 (2020): 1900130.

82. S. Wang and K. Lasn, "Integration of Optical Fibre Sensors by Material Extrusion 3-D Printing—The Effect of Bottom Interlayer Thickness," *Materials and Design* 221 (2022): 110914.

83. R.u Chen, W. He, H. Xie, and S. Liu, "Monitoring the strain and stress in FDM printed lamellae by using Fiber Bragg Grating sensors," *Polymer Testing* 93 (2021): 106944.

84. R. T. L. Ferreira, I. C. Amatte, T. A. Dutra, and D. Bürger, "Experimental Characterization and Micrography of 3D Printed PLA and PLA Reinforced with Short Carbon Fibers," *Composites Part B Engineering* 124 (2017): 88–100.

85. Y. G. Mittal, Y. Patil, P. P. Kamble, G. D. Gote, A. K. Mehta, and K. P. Karunakaran, "Warpage Control in Thermoplastic ABS Parts Produced Through Material Extrusion (MEX)-Based Fused Deposition Modeling (FDM)," *Rapid Prototyping Journal* 30 (2024): 1822–1835.

86. L. Xinhua, L. Shengpeng, L. Zhou, Z. Xianhua, C. Xiaohu, and W. Zhongbin, "An Investigation on Distortion of PLA Thin-Plate Part in the FDM Process," *International Journal of Advanced Manufacturing Technology* 79 (2015): 1117–1126.

87. M. S. Alsoufi and A. E. Elsayed, "Warping Deformation of Desktop 3D Printed Parts Manufactured by Open Source Fused Deposition Modeling (FDM) System," *International Journal of Mechanical and Mechatronics Engineering* 17 (2017): 7–16.

88. D. Foltut, E. Valean, V. Dzitac, and L. Marsavina, "The Influence of Temperature on the Mechanical Properties of 3D Printed and Injec-

tion Molded ABS," *Materials Today Proceedings* (Elsevier Ltd, 2022): 210–213.

89. M. Spoerk, J. Gonzalez-Gutierrez, J. Sapkota, S. Schuschnigg, and C. Holzer, "Effect of the Printing Bed Temperature on the Adhesion of Parts Produced by Fused Filament Fabrication," *Plastics, Rubber and Composites* 47 (2018): 17–24.

90. B. Akhoundi, M. Nabipour, F. Hajami, and D. Shakoori, "An Experimental Study of Nozzle Temperature and Heat Treatment (Annealing) Effects on Mechanical Properties of High-Temperature Polylactic Acid in Fused Deposition Modeling," *Polymer Engineering and Science* 60 (2020): 979–987.

91. F. Rivera-López, M. M. L. Pavón, E. C. Correa, and M. H. Molina, "Effects of Nozzle Temperature on Mechanical Properties of Polylactic Acid Specimens Fabricated by Fused Deposition Modeling," *Polymers* 16 (2024): 1867.

92. O. Ulkir, I. Ertugrul, S. Ersoy, and B. Yağımlı, "The Effects of Printing Temperature on the Mechanical Properties of 3D-Printed Acrylonitrile Butadiene Styrene," *Applied Sciences* 14 (2024): 3376.

93. G. V. Vlnogradov, G. M. Bartenev, A. I. El'kin, V. K. Mikhaylov, and S. A. Wear-Elsevier Sequoia, "Effect of Temperature on Friction and Adhesion of Crystalline Polymers," *Wear* 16 (1970): 213.

94. J. A. Forrest, K. Dalnoki-Veress, and J. R. Dutcher, "Interface and chain confinement effects on the glass transition temperature of thin polymer films,"*Physical Review E* 56 (1997): 5705–5716.

95. J. Loos, M. Tian, S. Rastogi, and P. J. Lemstra, "An Investigation on Chain Mobility in Solid State Polymer Systems," *Journal of Materials Science*, 35 (2000): 5147.

96. M. Coca-Gonzalez and M. Jimenez-Martinez, "Warpage: Causes, Manufacturing Processes and Future Challenges: A Review," *Proceedings of the Institution of Mechanical Engineers, Part L: Journal of Materials: Design and Applications* 239 (2024): 1201–1217.

97. H. Alzyod and P. Ficzere, "Material-Dependent Effect of Common Printing Parameters on Residual Stress and Warpage Deformation in 3D Printing: A Comprehensive Finite Element Analysis Study," *Polymers* 15 (2023): 2893.

98. P. Addepalli and S. Thirukkurungudi, www.ijert.org. n.d.

99. V. Ambade, S. Rajurkar, G. Awari, B. Yelamasetti, and S. Shelare, "Influence of FDM Process Parameters on Tensile Strength of Parts Printed by PLA Material," *International Journal on Interactive Design and Manufacturing* 19 (2023): 573–584.

100. B. Yu, G. Chen, J. Sun, et al., "Finite Element Analysis of Warping and Mechanical Properties of 3D Parts Printed by Fused Deposition Modeling," *Journal of Materials Engineering and Performance* 34 (2025): 2410–2423.

101. W. Shen, D. Veeramani, and H. Qin, "Warpage Mitigation Through Infill Sectioning in Fused Filament Fabrication," *IISE Transactions* (2024): 1–13.

102. M. V. Candal, I. Calafel, M. Fernández, et al., "Study of the Interlayer Adhesion and Warping During Material Extrusion-Based Additive Manufacturing of a Carbon Nanotube/Biobased Thermoplastic Polyurethane Nanocomposite," *Polymer* 224 (2021): 123734.

103. B. Thavornyutikarn, C. Aumnate, W. Kosorn, N. Nampichai, and W. Janvikul, "Acrylonitrile Butadiene Styrene/Thermoplastic Polyurethane Blends for Material Extrusion Three-Dimensional Printing: Effects of Blend Composition on Printability and Properties," *ACS Omega* 8 (2023): 45013–45025.

104. J. Yin, C. Lu, J. Fu, Y. Huang, and Y. Zheng, "Interfacial Bonding During Multi-Material Fused Deposition Modeling (FDM) Process Due to Inter-Molecular Diffusion," *Materials and Design* 150 (2018): 104–112.

105. A. S. de León, A. Domínguez-Calvo, and S. I. Molina, "Materials with Enhanced Adhesive Properties Based on Acrylonitrile-Butadiene-Styrene (ABS)/Thermoplastic Polyurethane (TPU) Blends for Fused Filament Fabrication (FFF)," *Materials and Design* 182 (2019): 108044.

106. V. Mishra, N. Bharat, V. Kumar, D. Veeman, and M. Vellaisamy, "Assessment of physio-mechanical characteristics of ABS/PETG blended parts fabricated by material extrusion 3D printing," *Physica Scripta* 99 (2024): 125033.

107. L. J. Love, V. Kunc, O. Rios, et al., "The Importance of Carbon Fiber to Polymer Additive Manufacturing," *Journal of Materials Research* 29 (2014): 1893–1898.

108. B. Nan, K. Wu, W. Chen, Y. Liu, and Q. Zhang, "Bioinspired Modification Strategy to Improve Thermal Conductivity of Flexible Poly (Vinyl Alcohol)/Nanodiamond Nanocomposite Films for Thermal Management Applications," *Applied Surface Science* 508 (2019): 144797.

109. P. Castelló-Pedrero, C. García-Gascón, and J. A. García-Manrique, "Multiscale Numerical Modeling of Large-Format Additive Manufacturing Processes Using Carbon Fiber Reinforced Polymer for Digital Twin Applications," *International Journal of Material Forming* 17 (2024): 15.

110. M. Sakagami, S. Ishiue, M. Kawaguchi, and A. Takezawa, "Reduction of the Residual Warpage of Fused Deposition Modeling by Negative Thermal Expansion Filler," *Materials and Design* 248 (2024): 113472.

111. M. Cocca, M. L. D. Lorenzo, M. Malinconico, and V. Frezza, "Influence of Crystal Polymorphism on Mechanical and Barrier Properties of Poly(L-Lactic Acid)," *European Polymer Journal* 47 (2011): 1073–1080.

112. M. L. Di Lorenzo, M. Cocca, and M. Malinconico, "Crystal Polymorphism of Poly(L-Lactic Acid) and its Influence on Thermal Properties," *Thermochimica Acta* 522 (2011): 110–117.

113. A. Elsayed, G. Melenka, and S. N. (Sunny) Leung, "Optimizing 3D Printing Parameters for Enhanced Electroactive PVDF Formation," in *Electroactive Polymer Actuators, Sensors, and Devices (EAPAD) 2025*, eds. J. D. Madden, A. L. Skov, S. S. Seelecke, and K. Takagi (SPIE, 2025), 31.

114. C. Silvestre, S. Cimmino, and E. Di Pace, "Morphology of polyolefins," in *Handbook of Polyolefins* (Marcel Dekker Inc, 2000), 175–206.

115. M. Cocca, R. Androsch, M. C. Righetti, M. Malinconico, and M. L. Di Lorenzo, "Conformationally Disordered Crystals and Their Influence on Material Properties: The Cases of Isotactic Polypropylene, Isotactic Poly(1-Butene), and Poly(L-Lactic Acid)," *Journal of Molecular Structure* 1078 (2014): 114–132.

116. D. Zhang, L. Ding, F. Yang, F. Lan, Y.a Cao, and M. Xiang, "Structural evolution of β-iPP with different supermolecular structures during the simultaneous biaxial stretching process," *Polymer Journal* 53 (2021): 331–344.

117. D. Sawai, Y. Tsugane, M. Tamada, T. Kanamoto, M. Sungil, and S.-H. Hyon, "Crystal Density and Heat of Fusion for a Stereo-Complex of Poly(L -Lactic Acid) and Poly(D -Lactic Acid)," *Journal of Polymer Science: Polymer Physics* 45 (2007): 2632–2639.

118. T. L. Nguyen, F. Bédoui, P.-E. Mazeran, and M. Guigon, "Mechanical Investigation of Confined Amorphous Phase in Semicrystalline Polymers: Case of PET and PLA," *Polymer Engineering and Science* 55 (2015): 397–405.

119. C. H. Bamford and A. D. Jenkins, "Termination Reaction in Vinyl Polymeriza-tion : Preparation of Block Copolymers," *Nature* 176 (1955): 78.

120. H. Chen and P. Cebe, "Investigation of the Rigid Amorphous Fraction in Nylon-6," *Journal of Thermal Analysis and Calorimetry* 89 (2007): 417–425.

121. N. S. Yenikolopyan, L. N. Raspopov, A. D. Pomogailo, et al., "Structure and Density of the Amorphous and Crystalline Phases in Low-Density Linear Polyethylenes," *Polymer Science U.S.S.R* 31 (1989): 2882–2891.

122. T. D. Fornes and D. R. Paul, "Crystallization Behavior of Nylon 6 Nanocomposites," *Polymer* 44 (2003): 3945–3961.

123. D. R. Holmes, C. W. Bunn, and D. J. Smith, "The Crystal Structure of Polycaproamide: Nylon 6," *Journal of Polymer Science* 17 (1955): 159–177.

124. C. S. Abbott, M. Sperry, and N. B. Crane, "Relationships Between Porosity and Mechanical Properties of Polyamide 12 Parts Produced Using the Laser Sintering and Multi-Jet Fusion Powder Bed Fusion Processes," *Journal of Manufacturing Processes* 70 (2021): 55–66.

125. S. Ebnesajjad, "Introduction to fluoropolymers: Materials, technology, and applications," in *Plastics Design Library* (William Andrew, 2020).

126. P. Gkertzos, A. Kotzakolios, G. Mantzouranis, and V. Kostopoulos, "Nozzle Temperature Calibration in 3D Printing," *International Journal on Interactive Design and Manufacturing* 18 (2024): 879–899.

127. M. L. Di Lorenzo, S. Liparoti, D. Cavallo, T. Hashemi, and R. Pantani, "Fused Filament Fabrication of Poly(L-Lactic Acid): A Thermal Analysis Approach to Optimize Processing Conditions," *International Journal of Polymer Science* 2025 (2025): 1–13.

128. M. S. Cadete, T. E. P. Gomes, I. Gonçalves, and V. Neto, "Influence of 3D-printing deposition parameters on crystallinity and morphing properties of PLA-based materials," *Progress in Additive Manufacturing* 10 (2024): 127–137.

129. L. Wang, W. M. Gramlich, and D. J. Gardner, "Improving the impact strength of Poly(lactic acid) (PLA) in fused layer modeling (FLM)," *Polymer* 114 (2017): 242–248.

130. J. X. Li and W. L. Cheung, "Conversion of growth and recrystallisation of b-phase in doped iPP," *Polymer* 40 (1999): 2085–2088.

131. L. Wang, J. E. Sanders, D. J. Gardner, and Y. Han, "Effect of Fused Deposition Modeling Process Parameters on the Mechanical Properties of a Filled Polypropylene," *Progress in Additive Manufacturing* 3 (2018): 205–214.

132. C. Benwood, A. Anstey, J. Andrzejewski, M. Misra, and A. K. Mohanty, "Improving the Impact Strength and Heat Resistance of 3D Printed Models: Structure, Property, and Processing Correlationships during Fused Deposition Modeling (FDM) of Poly(Lactic Acid)," *ACS Omega* 3 (2018): 4400–4411.

133. M. Harris, J. Potgieter, R. Archer, and K. M. Arif, "In-Process Thermal Treatment of Polylactic Acid in Fused Deposition Modelling," *Materials and Manufacturing Processes* 34 (2019): 701–713.

134. H. Vanaei, M. Shirinbayan, M. Deligant, et al., "Influence of Process Parameters on Thermal and Mechanical Properties of Polylactic Acid Fabricated by Fused Filament Fabrication," *Polymer Engineering and Science* 60 (2020): 1822–1831.

135. L. Wang and D. J. Gardner, "Contribution of Printing Parameters to the Interfacial Strength of Polylactic Acid (PLA) in Material Extrusion Additive Manufacturing," *Progress in Additive Manufacturing* 3 (2018): 165–171.

136. M. L. Di Lorenzo and R. Androsch, "Crystallization of Poly(Lactic Acid)," in *Biodegradable Polyesters* (Wiley Blackwell, 2015), 109–130.

137. A. Gałeski, Z. Bartczak, and M. Pracella, "Spherulite Nucleation in Polypropylene Blends with Low Density Polyethylene," *Polymer* 25 (1984): 1323–1326.

138. Y. Liao, C. Liu, B. Coppola, et al., "Effect of Porosity and Crystallinity on 3D Printed PLA Properties," *Polymers* 11 (2019): 1487.

139. B. Valentan, Ž. Kadivnik, T. Brajlih, et al., "Processing Poly(Ether Etherketone) on A 3D Printer For Thermoplastic Modelling", *Materials and technology* 47 (2013): 715–721.

140. P. Sikder, B. T. Challa, and S. K. Gummadi, "A Comprehensive Analysis on the Processing-Structure-Property Relationships of FDM-Based 3-D Printed Polyetheretherketone (PEEK) Structures," *Materialia* 22 (2022): 101427.

141. A. Maloney, I. Major, N. Gately, and D. M. Devine, "Effects of 3D Printing Parameters on the Flexural Properties of Semi-Crystalline PEKK," *Materials Today Communications* 42 (2025): 111152.

142. J. Han, J. Tong, X. Tian, L. Xia, and D. Ma, "Thermal Simulation and Warping Deformation Experimental Study of PEEK in Material Extrusion," *Macromolecular Theory and Simulations* 30 (2021): 2000055.

143. A. Nogales, E. Gutiérrez-Fernández, M. C. García-Gutiérrez, et al., "Structure Development in Polymers during Fused Filament Fabrication (FFF): An in Situ Small- And Wide-Angle X-Ray Scattering Study Using Synchrotron Radiation," *Macromolecules* 52 (2019): 9715–9723.

144. G. Allegra and I. W. Bassi, "Isomorphism in Synthetic Macromolecular Systems," in *Fortschritte Der Hochpolymeren-Forschung* (Springer Berlin Heidelberg, 1969), 549–574.

145. Y. Yu, L. Sang, Z. Wei, X. Leng, and Y. Li, "Unique Isodimorphism and Isomorphism Behaviors of Even-Odd Poly(Hexamethylene Dicarboxylate) Aliphatic Copolyesters," *Polymer* 115 (2017): 106–117.

146. G. Ceccorulli, M. Scandola, A. Kumar, B. Kalra, and R. A. Gross, "Cocrystallization of Random Copolymers of ω-Pentadecalactone and ε-Caprolactone Synthesized by Lipase Catalysis," *Biomacromolecules* 6 (2005): 902–907.

147. S. Li and R. A. Register, "Crystallization in Copolymers," in *Handbook of Polymer Crystallization*, (Wiley & Sons, Inc., 2013): 327–346, https://onlinelibrary.wiley.com/doi/.

148. G. Spiegel and C. Paulik, "Polypropylene Copolymers Designed for Fused Filament Fabrication 3D-Printing," *Macromolecular Reaction Engineering* 14 (2020): 1900044.

149. M. L. Di Lorenzo, "Crystallization of Poly(ethylene terephthalate): A Review," *Polymers* 16 (2024): 1975.

150. S. Valvez, A. P. Silva, and P. N. B. Reis, "Optimization of Printing Parameters to Maximize the Mechanical Properties of 3D-Printed PETG-Based Parts," *Polymers* 14 (2022): 2564.

151. D. Fico, D. Rizzo, R. Casciaro, and C. E. Corcione, "A Review of Polymer-Based Materials for Fused Filament Fabrication (FFF): Focus on Sustainability and Recycled Materials," *Polymers* 14 (2022): 465.

152. A. R. Zanjanijam, I. Major, J. G. Lyons, U. Lafont, and D. M. Devine, "Fused Filament Fabrication of Peek: A Review of Process-Structure-Property Relationships," *Polymers* 12 (2020): 1665.

153. C.-Y. Liaw, J. W. Tolbert, L. W. Chow, and M. Guvendiren, "Interlayer Bonding Strength of 3D Printed PEEK Specimens," *Soft Matter* 17 (2021): 4775–4789.

154. L. Doyle, X. Pérez-Ferrero, J. García-Molleja, R. Losada, P. Romero-Rodríguez, and J. P. Fernández-Blázquez, "Fused Filament Fabrication of Slow-Crystallizing Polyaryletherketones: Crystallinity and Mechanical Properties Linked to Processing and Post-Treatment Parameters," *Polymers* 16 (2024): 3354.

155. M. Regis, A. Bellare, T. Pascolini, and P. Bracco, "Characterization of thermally annealed PEEK and CFR-PEEK composites: Structure-properties relationships," *Polymer Degradation and Stability* 136 (2017): 121–130.

156. Z. Bartczak, A. Galeski, and N. P. Krasnikova, "Primary Nucleation and Spherulite Growth Rate in Isotactic Polypropylene-Polystyrene Blends," *Polymer* 28 (1987): 1627–1634.

157. M. L. Di Lorenzo, "Poly(<scp>l</scp>-Lactic Acid)/Poly(Butylene Succinate) Biobased Biodegradable Blends," *Polymer Reviews* 61 (2021): 457–492.

158. M. L. Di Lorenzo, S. Cimmino, and C. Silvestre, "Nonisothermal crystallization of isotactic polypropylene blended with poly(α-pinene). 2. Growth rates," *Macromolecules* 33 (2000): 3828–3832.

159. M. L. Di Lorenzo, "Spherulite Growth Rates in Binary Polymer Blends," *Progress in Polymer Science* 28 (2003): 663–689.

160. Q. B. Ho and M. Kontopoulou, "Improving the Adhesion and Properties in the Material Extrusion of Polypropylene by Blending with a Polyolefin Elastomer," *Additive Manufacturing* 55 (2022): 102818.

161. N. E. Zander, M. Gillan, Z. Burckhard, and F. Gardea, "Recycled Polypropylene Blends as Novel 3D Printing Materials," *Additive Manufacturing* 25 (2019): 122–130.

162. A. Slonov, I. Musov, A. Zhansitov, et al., "Investigation of the Properties of Polyethylene and Ethylene-Vinyl Acetate Copolymer Blends for 3D Printing Applications," *Polymers* 15 (2023): 4129.

163. Y. Jia, H. He, X. Peng, S. Meng, J. Chen, and Y.i Geng, "Preparation of a New Filament Based on Polyamide-6 for Three-Dimensional Printing," *Polymer Engineering and Science* 57 (2017): 1322–1328.

164. I. Farina, N. Singh, F. Colangelo, R. Luciano, G. Bonazzi, and F. Fraternali, "High-Performance Nylon-6 Sustainable Filaments for Additive Manufacturing," *Materials* 12 (2019): 3955.

165. G. Wypych, *Handbook of Nucleating Agents* (Elsevier, 2021).

166. A. Patel and M. Taufik, "Advances in Nanocomposite Material for Fused Filament Fabrication," *Polymer-Plastics Technology and Materials* 61 (2022): 1617–1661.

167. K. Chen, L. Yu, Y. Cui, M. Jia, and K. Pan, "Optimization of Printing Parameters of 3D-Printed Continuous Glass Fiber Reinforced Polylactic Acid Composites," *Thin-Walled Structures* 164 (2021): 107717.

168. O. S. Carneiro, A. F. Silva, and R. Gomes, "Fused Deposition Modeling with Polypropylene," *Materials and Design* 83 (2015): 768–776.

169. M. Ahmadifar, K. Benfriha, and M. Shirinbayan, "Thermal, Tensile and Fatigue Behaviors of the PA6, Short Carbon Fiber-Reinforced PA6, and Continuous Glass Fiber-Reinforced PA6 Materials in Fused Filament Fabrication (FFF)," *Polymers* 15 (2023): 507.

170. J. Bochnia, M. Blasiak, and T. Kozior, "Tensile Strength Analysis of Thin-Walled Polymer Glass Fiber Reinforced Samples Manufactured by 3D Printing Technology," *Polymers* 12 (2020): 2783.

171. A. E. Magri, K. El Mabrouk, S. Vaudreuil, and M. E. Touhami, "Mechanical Properties of CF-Reinforced PLA Parts Manufactured by Fused Deposition Modeling," *Journal of Thermoplastic Composite Materials* 34 (2021): 581–595.

172. M. Heidari-Rarani, M. Rafiee-Afarani, and A. M. Zahedi, "Mechanical Characterization of FDM 3D Printing of Continuous Carbon Fiber Reinforced PLA Composites," *Composites, Part B Engineering* 175 (2019): 107147.

173. X. Tian, T. Liu, C. Yang, Q. Wang, and D. Li, "Interface and Performance of 3D Printed Continuous Carbon Fiber Reinforced PLA Composites," *Composites Part A: Applied Science and Manufacturing* 88 (2016): 198–205.

174. G. D. Goh, V. Dikshit, A. P. Nagalingam, et al., "Characterization of Mechanical Properties and Fracture Mode of Additively Manufactured Carbon Fiber and Glass Fiber Reinforced Thermoplastics," *Materials and Design* 137 (2018): 79–89.

175. A. N. Dickson, J. N. Barry, K. A. McDonnell, and D. P. Dowling, "Fabrication of Continuous Carbon, Glass and Kevlar Fibre Reinforced Polymer Composites Using Additive Manufacturing," *Additive Manufacturing* 16 (2017): 146–152.

176. E. Yasa and K. Ersoy, "Dimensional Accuracy and Mechanical Properties of Chopped Carbon Reinforced Polymers Produced by Material Extrusion Additive Manufacturing," *Materials* 12 (2019): 3885.

177. C. Savandaiah, J. Maurer, M. Gall, A. Haider, G. Steinbichler, and J. Sapkota, "Impact of Processing Conditions and Sizing on the Thermomechanical and Morphological Properties of Polypropylene/Carbon Fiber Composites Fabricated by Material Extrusion Additive Manufacturing," *Journal of Applied Polymer Science* 138 (2021): 50243.

178. F. Casamento, E. Padovano, S. Pappalardo, A. Frache, and C. Badini, "Development of Polypropylene-Based Composites Through Fused Filament Fabrication: The Effect of Carbon-Based Fillers," *Composites Part A: Applied Science and Manufacturing* 164 (2023): 107308.

179. X. Han, D. Yang, C. Yang, et al., "Carbon Fiber Reinforced PEEK Composites Based on 3D-Printing Technology for Orthopedic and Dental Applications," *J Clin Med* 8 (2019): 240.

180. R. Singh, R. Kumar, and I. Ahuja, "Mechanical, Thermal and Melt Flow of Aluminum-Reinforced PA6/ABS Blend Feedstock Filament for Fused Deposition Modeling," *Rapid Prototyping Journal* 24 (2018): 1455–1468.

181. R. Kumar, R. Singh, and I. P. S. Ahuja, "Investigations of Mechanical, Thermal and Morphological Properties of FDM Fabricated Parts for Friction Welding Applications," *Measurement* 120 (2018): 11–20.

182. Z. Luo and Y. Zhao, "A survey of finite element analysis of temperature and thermal stress fields in powder bed fusion Additive Manufacturing," *Additive Manufacturing* 21 (2018): 318–332.

183. M. Zafar, A. Bakhshi, and M. Hojati, "Toward 3D-Printable Engineered Cementitious Composites: Mix Design Proportioning, Flowability, and Mechanical Performance," *Proceedings* (2022).

184. M. Hojati, M. Saeed Zafar, and A. Bakhshi, Evaluation of Fresh and Hardened Properties of 3D-Printed Engineered Cementitious Composites (ECC) Designed for Sustainable and Resilient Infrastructure Systems, (2022), https://repository.lsu.edu/transet_data/156.

185. F. Montevecchi, G. Venturini, N. Grossi, A. Scippa, and G. Campatelli, "Idle Time Selection for Wire-Arc Additive Manufacturing: A Finite Element-Based Technique," *Additive Manufacturing* 21 (2018): 479–486.

186. K. M. B. Jansen and G. Titomanlio, "Effect of Pressure History on Shrinkage and Residual Stresses—Injection Molding with Constrained Shrinkage," *Polymer Engineering and Science* 36 (1996): 2029–2040.

187. Z. Pluta and T. Hryniewicz, "A Developed Version of the Hooke's Law, International Letters of Chemistry," *Physics and Astronomy* 7 (2013): 49–59.

188. T.-M. Wang, J.-T. Xi, and Y. Jin, "A Model Research for Prototype Warp Deformation in the FDM Process," *The International Journal of Advanced Manufacturing Technology* 33 (2007): 1087–1096.

189. B. Wijnen, P. Sanders, and J. M. Pearce, "Improved Model and Experimental Validation of Deformation in Fused Filament Fabrication of Polylactic Acid," *Progress in Additive Manufacturing* 3 (2018): 193–203.

190. B. Ergene and Ç. Bolat, "Simulation of Fused Deposition Modeling of Glass Fiber Reinforced ABS Impact Samples: The Effect of Fiber Ratio, Infill Rate, and Infill Pattern on Warpage and Residual Stresses," *Hittite Journal of Science and Engineering* 10 (2023): 21–31.

191. B. Jiang, Y. Chen, L. Ye, L. Chang, and H. Dong, "Residual Stress and Warpage of Additively Manufactured SCF/PLA Composite Parts," *Advanced Manufacturing: Polymer and Composites Science* 9 (2023).

192. N. Watanabe, M. L. Shofner, N. D. Treat, D. W. Rosen, and G. W. Woodruff, "A Model For Residual Stress And Part Warpage Prediction In Material Extrusion With Application To Polypropylene," in: *2016: Proceedings of the 26th Annual International Solid Freeform Fabrication Symposium – An Additive Manufacturing Conference* (University of Texas, 2016).

193. A. A. Samy, A. Golbang, E. Harkin-Jones, E. Archer, D. Tormey, and A. Mcilhagger, "Finite Element Analysis of Residual Stress and Warpage in a 3D Printed Semi-Crystalline Polymer: Effect of Ambient Temperature and Nozzle Speed," *Journal of Manufacturing Processes* 70 (2021): 389–399.

194. G. Chen, D. Wang, W. Hua, et al., "Simulating and Predicting the Part Warping in Fused Deposition Modeling by Thermal-Structural Coupling Analysis," *3D Printing and Additive Manufacturing* 10 (2023): 70–82.

195. Y. Zhang and K. Chou, "A Parametric Study of Part Distortions in Fused Deposition Modelling Using Three-Dimensional Finite Element Analysis," *Proceedings of the Institution of Mechanical Engineers Part B: Journal of Engineeing Manufacture* 222 (2008): 959–968.

196. A. Cattenone, S. Morganti, G. Alaimo, and F. Auricchio, "Finite Element Analysis of Additive Manufacturing Based on Fused Deposition Modeling (FDM): Distortion Prediction and Comparison with Experimental Data," *Journal of Manufacturing Science and Engineering* 141 (2018): 011010.

197. D. Banerjee and S. Mishra, "A Numerical Study on Warpage Deformation of Fused Deposition Modelling Built parts," *International Journal of Mechanical Engineering* 7 (2022): 974–5823.

198. D. Syrlybayev, B. Zharylkassyn, A. Seisekulova, A. Perveen, and D. Talamona, "Optimization of the Warpage of Fused Deposition Modeling Parts Using Finite Element Method," *Polymers* 13 (2021): 3849.

199. Y. Zhang and Y. Chou, "3D FEA Simulations of Fused Deposition Modeling Process," in *International Manufacturing Science and Engineering Conference (MSEC)* (ASME, 2006), 1121–1128.